Zircon and monazite reveal late Cambrian/early Ordovician partial melting of the Central Seve Nappe Complex, Scandinavian Caledonides

Christopher J. Barnes[1] · Michał Bukała[1] · Riccardo Callegari[2,3] · Katarzyna Walczak[2] · Ellen Kooijman[4] ·
Melanie Kielman-Schmitt[4] · Jarosław Majka[2,3]

Abstract

The Seve Nappe Complex (SNC) comprises continental rocks of Baltica that were subducted and exhumed during the Caledonian orogeny prior to collision with Laurentia. The tectonic history of the central SNC is investigated by applying *in-situ* zircon and monazite (Th-)U–Pb geochronology and trace element analysis to (ultra-)high pressure (UHP) paragneisses in the Avardo and Marsfjället gneisses. Zircons in the Avardo Gneiss exposed at Sippmikk creek exhibit xenocrystic cores with metamorphic rims. Cores show typical igneous REE profiles and were affected by partial Pb-loss. The rims have flat HREE profiles and are interpreted to have crystallized at 482.5 ± 3.7 Ma during biotite-dehydration melting and peritectic garnet growth. Monazites in the paragneiss are chemically homogeneous and record metamorphism at 420.6 ± 2.0 Ma. In the Marsfjället Gneiss exposed near Kittelfjäll, monazites exhibit complex zoning with cores enveloped by mantles and rims. The cores are interpreted to have crystallized at 481.6 ± 2.1 Ma, possibly during garnet resorption. The mantles and rims provide a dispersion of dates and are interpreted to have formed by melt-driven dissolution-reprecipitation of pre-existing monazites until 463.1 ± 1.8 Ma. Depletion of Y, HREE, and U in the mantles and rims compared to the cores record peritectic garnet and zircon growth. Altogether, the Avardo and Marsfjället gneisses show evidence of late Cambrian/early Ordovician partial melting (possibly in (U)HP conditions), Middle Ordovician (U)HP metamorphism, and late Silurian tectonism. These results indicate that the SNC underwent south-to-north oblique subduction in late Cambrian time, followed by progressive north-to-south exhumation to crustal levels prior to late Silurian continental collision.

Introduction

The Scandinavian Caledonides is an excellent natural laboratory for studying Wilson-cycle tectonics. It comprises several allochthons that altogether record Neoproterozoic opening of the Iapetus Ocean, followed by closure of the ocean starting in late Cambrian time, progressing to Silurian to Devonian collision of Baltica and Laurentia (Gee et al. 1985, 2008, 2020; Stephens and Gee 1985; Stephens 1988; Roberts 2003; Corfu et al. 2014; Stephens et al. 2020). An important element for understanding the evolution of the Scandinavian Caledonides is the Seve Nappe Complex (SNC), which is traditionally regarded to be remnants of the Baltican passive margin that were subducted to mantle depths during Iapetus Ocean closure (Andréasson 1994; Gee et al. 2020). The SNC comprises metasedimentary rocks that host amphibolites,

✉ Christopher J. Barnes
cjbarnes063@gmail.com

1   Institute of Geological Sciences, Polish Academy of Sciences, Krakow, Poland

2   Faculty of Geology, Geophysics, and Environmental Protection, AGH University of Science and Technology, Krakow, Poland

3   Department of Earth Sciences, Uppsala University, Uppsala, Sweden

4   Department of Geosciences, Swedish Museum of Natural History, Stockholm, Sweden

eclogites, peridotites, and pyroxenites recording (ultra-) high pressure metamorphism (e.g., Janák et al. 2013; Majka et al. 2014a; Gilio et al. 2015; Klonowska et al. 2016, 2017; Bukała et al. 2018, 2020a; Petrík et al. 2019). It is divided into several (U)HP terranes > 1000 km along strike of the Scandinavian Caledonides, and are often grouped as the northern, central and west-central SNC terranes. The record of (U)HP metamorphism has often been discussed to be older for the northern terranes (late Cambrian/early Ordovician metamorphism; Root and Corfu 2012; Barnes et al. 2021a; Fassmer et al. 2021) versus the central and west-central SNC (Middle Ordovician metamorphism; Brueckner and Van Roermund 2007; Fassmer et al. 2017). The apparently different temporal (U)HP records have led to tectonic models involving diachronous subduction of the Baltican margin, either progressing from north to the south through time, or reflecting a promontory in the north that was subducted prior to the southern portions of the margin (Brueckner and Van Roermund 2004; Bukała et al. 2018; Fassmer et al. 2021). Further understanding and evaluation of these models is critical for unraveling the evolution of the Scandinavian Caledonides and Iapetus Ocean closure.

Zircon and monazite are two important refractory minerals in metasedimentary rocks that can record a wide range of sub and suprasolidus metamorphic reactions (e.g., Engi 2017; Rubatto 2017). The metamorphic records of the central SNC have predominantly been extracted from (U)HP mafic and ultramafic lithologies hosted within metasedimentary rocks. However, recent studies demonstrate that zircon and monazite often record older metamorphic histories than those preserved in the mafic and ultramafic lithologies (Barnes et al. 2019, 2021b; Petrík et al. 2019; Walczak et al. 2021). In particular, zircon geochronology of the Tväråklumparna Gneiss in the west-central SNC (Walczak et al. 2021) and monazite geochronology of the Marsfjället Gneiss in the central SNC (Petrík et al. 2019) indicate late Cambrian/early Ordovician (U)HP metamorphism and partial melting of the SNC terranes that were previously thought to have only undergone Middle Ordovician (U)HP metamorphism. Following these discoveries, *in-situ* zircon and monazite geochronology and trace element analysis are applied to paragneisses of the central SNC that host Middle Ordovician mafic and ultramafic (U)HP lithologies in order to expand the tectonic history of these terranes. The results are compared within the broader history of the SNC to test previous models for subduction of the Baltican margin during Iapetus Ocean closure.

Geological background

The (U)HP metamorphic terranes of the Seve Nappe Complex are generally grouped as the northern SNC (Vaimok Lens, Tsäkkok Lens, Mårma Terrane; Root and Corfu 2012; Bukała et al. 2018, 2020a; Andréasson et al. 2018; Fassmer et al. 2021), the central SNC (Svartsjöbäcken Schists, Marsfjället Gneiss, Avardo Gneiss, Sjouten Unit; Brueckner et al. 2004; Brueckner and Van Roermund, 2007; Majka et al. 2012; Janák et al. 2013; Gilio et al. 2015; Grimmer et al. 2015; Klonowska et al. 2016; Fassmer et al. 2017; Petrík et al. 2019), and the west-central SNC (Åreskutan Gneiss, Tväråklumparna Gneiss; Majka et al. 2012; Majka et al. 2014a, b; Klonowska et al. 2017; Walczak et al. 2021).

The central SNC is further divided into the Western, Central, and Eastern belts (Fig. 1A; Trouw 1973; Williams and Zwart 1977; Zachrisson and Sjöstrand 1990). The Western Belt is referred to as the Svartsjöbäcken Schists, which are dominated by garnet white mica schists, locally kyanite-bearing, which host garnet amphibolites (Trouw 1973). Pressure–temperature (P–T) conditions of the schists were calculated to > 1.5 GPa and 670 ± 30 °C, with garnet Sm–Nd geochronology establishing the timing of subduction to 462.0 ± 3.5 Ma (Grimmer et al. 2015).

The Marsfjället Gneiss constitutes the Central Belt that underlies the Svartsjöbäcken Schists (Fig. 1A). The contact between the units has been described as metamorphic facies transition corresponding to the appearance of ubiquitous kyanite within the rocks (Trouw 1973). The Marsfjället Gneiss consists of garnet- and kyanite-bearing pelitic and quartzo-feldspathic metasedimentary rocks that host garnet amphibolites and ultramafic rocks. Paragneisses of the Marsfjället Gneiss exposed near Saxnäs contain metamorphic microdiamonds included in garnet, providing direct evidence of UHP metamorphism. The timing of metamorphism was interpreted to be 472 ± 3 Ma, provided by monazite Th–U–total Pb geochronology (Fig. 1B; Petrík et al. 2019). In contrast, the paragneisses and amphibolites near Kittelfjäll, ~ 30 km northeast of Saxnäs, demonstrate that the Marsfjället Gneiss underwent partial melting at 474.2 ± 9.6 Ma, yielded by zircon U–Pb geochronology (Bukała et al. 2020b). Orogenic spinel peridotites are exposed close to the Kittelfjäll paragneisses and preserve metamorphic conditions of 650–830 °C and 1–2 GPa during subduction, followed by exhumation of the peridotite to 550–600 °C and 0.45–0.60 GPa (Clos et al. 2014). White mica Rb–Sr geochronology resolved exhumation of the Svartsjöbäcken Schists and Marsfjället Gneiss to 433.2 ± 4.8 Ma (Grimmer et al. 2015).

The Central Belt further consists of the Lillfjället Gneiss, the Avardo Gneiss, and the Lejaren Unit (Fig. 1A; Zachrisson and Sjöstrand, 1990). The Lillfjället Gneiss and the
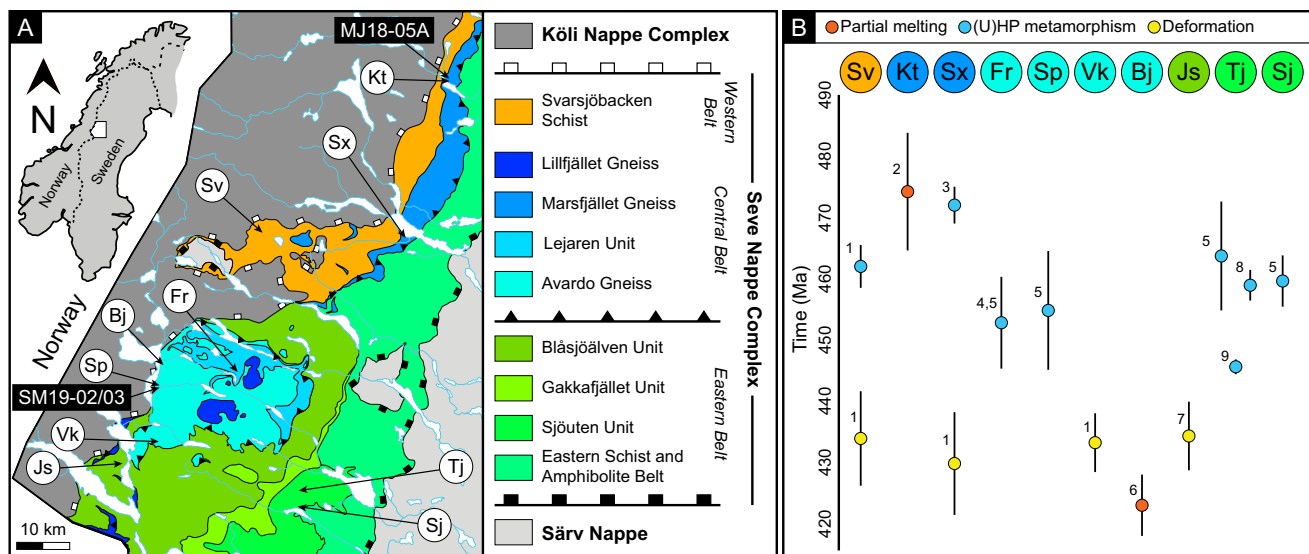
Fig. 1 A Tectonostratigraphic map of the southern Västerbotten and northern Jämtland (modified after Zachrisson and Sjöstrand 1990) highlighting the Seve Nappe Complex subdivisions. Several key localities of (U)HP rocks and locations of previous geochronological analyses are indicated by the abbreviations in white circles. The sample locations of the Sippmikk paragneiss samples (SM19-02: 64°44′30.52″N, 14°14′32.79″E; SM19-03: 64°44′30.47″N, 14°14′33.95″E) and the Kittelfjäll paragneiss sample (MJ18-05A: 65°15′10.75″N, 15°25′13.06″E) are presented. **B** Summary of previous geochronological studies throughout the SNC in the area of the tectonostratigraphic map coverage. The ages (±2σ uncertainty) are color coded according to their original interpretations. The abbreviations are color coded according to their tectonostratigraphic position in the SNC, according to the map legend. Abbreviations from left to right are: *Sv* Svartsjöbäcken, *Kt* Kittelfjäll, *Sx* Saxnäs, *Fr* Friningen, *Sp* Sippmikk, *Vk* sample VAK of Grimmer et al. (2015), *Bj* Blåsjön, *Js* Jormsjön, *Tj* Tjeliken, *Sj* Stour Jougdan. References for previous geochronology: [1]Grimmer et al. (2015); [2]Bukała et al. (2020b); [3]Petrík et al. (2019); [4]Brueckner et al. (2004); [5]Brueckner and Van Roermund (2007); [6]Williams and Claesson (1987); [7]Dallmeyer and Gee (1988); [8]Fassmer et al. (2017); [9]Root and Corfu (2012)

Avardo Gneiss are both characterized by kyanite-sillimanite-garnet metapelites with quartzites and quartzo-feldspathic rocks and show evidence of partial melting (Van Roermund and Bakker 1983). The two gneisses are distinguished as the latter hosts eclogites and ultramafic rocks, whereas the former contains amphibolites. The Lejaren Unit is predominantly composed of quartzo-feldspathic rocks that host amphibolites and ultramafic rocks. The quartzo-feldspathic rocks generally show evidence of partial melting but apparently do not bear abundant metamorphic index minerals (Van Roermund and Bakker 1983). Of the three, the Avardo Gneiss has been the focus of investigation due to several key localities of eclogite as well as orogenic peridotites and pyroxenites, some of which are garnet-bearing (Van Roermund 1989). Mineral assemblages of the metasedimentary rocks indicate two distinct HP events as two different kyanite generations have been identified (Van Roermund and Bakker 1983). First evidence of UHP metamorphism in the Avardo Gneiss (and in the SNC as a whole) was obtained from an eclogitized portion of a garnet pyroxenite dyke within a garnet peridotite exposure in the Avardo Gneiss northeast of Lake Friningen that yielded conditions of ~3 GPa and ~800 °C (Janák et al. 2013). These conditions were reproduced by the garnet peridotite (Gilio et al. 2015). Garnet Sm–Nd geochronology of garnet pyroxenite yielded

452.8 ± 7.5 Ma, 452 ± 20 Ma and 448 ± 17 Ma, interpreted as the timing of peak metamorphism (Fig. 1B; Brueckner et al. 2004; Brueckner and Van Roermund 2007). Eclogite exposures at Sippmikk creek have yielded minimum P–T conditions of ~1.8 GPa and ~750 °C (Van Roermund 1985). Garnet Sm–Nd geochronology from eclogite indicates its formation at 454.8 ± 9.7 Ma (Brueckner and Van Roermund 2007), similar to the Friningen garnet pyroxenite. White mica Rb–Sr geochronology of the Avardo Gneiss resolved exhumation to 433.2 ± 4.8 Ma (Grimmer et al. 2015) and zircon U–Pb geochronology applied to leucosomes of partially melted metasedimentary rocks yielded 423 ± 5 Ma (Fig. 1B; Williams and Claesson 1987).

The Central Belt is separated from the underlying Eastern Belt by a distinct mylonitic zone that represents a tectonic contact (Fig. 1A; Trouw 1973; Van Roermund and Bakker 1983). In the northern exposures, the Eastern Belt is also referred to as the Eastern Schist and Amphibolite Belt. Schists of variable composition dominate with subordinate amphibolite layers and lenses throughout (Trouw, 1973). To the southwest, the Eastern Belt also comprises the Blåsjöälvan Unit, the Gakkafjället Unit, and the Sjouten Unit (Zachrisson and Sjöstrand 1990), which collectively overly the Eastern Schist and Amphibolite Belt (Fig. 1A). The Blåsjöälvan Unit is dominated by amphibolites, often

garnet-bearing, in addition to less frequent dolerites, paragneisses and mica schists. Mylonitic amphibolites in the upper parts of the unit in contact with the Avardo Gneiss, exposed near Lake Blåsjön, yielded hornblende $^{40}Ar/^{39}Ar$ dates in the range of c. 436–432 Ma (Dallmeyer and Gee 1988). The Gakkafjället Unit and underlying Sjouten Unit are both dominated by quartzo-feldspathic gneisses and garnet mica schists, however, they are distinguished as the former hosts amphibolites and metagabbros and typically preserves amphibolite-facies mineral assemblages, whereas the latter contains numerous eclogites and ultramafic lithologies, including garnet peridotite and pyroxenite, indicating (U)HP metamorphic conditions (Van Roermund and Bakker 1983; Van Roermund 1985, 1989; Majka et al. 2014b; Klonowska et al. 2016; Fassmer et al. 2017).

Two key localities have been studied in the Sjouten Unit, at Tjeliken Mountain and on the northern shores of Stor Jougdan. At Tjeliken, eclogites and gneisses preserve P–T conditions of 2.5–2.7 GPa and 650–750 °C (Majka et al. 2014b). Garnet Sm–Nd geochronology of the eclogites yielded 463.7 ± 8.9 Ma (Fig. 1B; Brueckner and Van Roermund 2007), similar to the age of (U)HP metamorphism recorded by the Avardo Gneiss pyroxenite and eclogite. Root and Corfu (2012) questioned the age as their results of zircon U–Pb geochronology of the Tjeliken eclogite produced 445.6 ± 1.2 Ma, which was also reproduced by two individual rutile U–Pb dates of 445.0 ± 2.4 Ma and 446.3 ± 3.7 Ma. Subsequent garnet Lu–Hf geochronology of the eclogite and zircon U–Pb geochronology of the host paragneiss provided 458.1 ± 1.0 Ma and 458.9 ± 2.5 Ma, supporting the previous garnet Sm–Nd results for the timing of UHP metamorphism and suggesting the eclogite zircon and rutile may record exhumation (Fassmer et al. 2017). Conditions for UHP metamorphism are also preserved by eclogite and garnet pyroxenite at Stor Jougdan, which collectively constrain the metamorphic conditions to 2.3–4.0 GPa and 750–960 °C (Klonowska et al. 2016). Garnet Sm–Nd geochronology conducted on garnet peridotite from Stor Jougdan, produced 459.6 ± 4.2 Ma (Fig. 1B; Brueckner and Van Roermund, 2007).

Methods

Microscopy and mineral chemistry

Three paragneiss samples were investigated for this study (Fig. 1A). Two were obtained from the Sippmikk creek exposure of the Avardo Gneiss (samples SM19-02, and SM19-03) and one was obtained from a roadcut exposure of the Marsfjället Gneiss northwest of the town of Kittelfjäll (sample MJ18-05A), which was previously studied by Bukała et al. (2020b). All paragneisses were investigated

using transmitted light microscopy to characterize mineral assemblages, textural relationships, and microstructures. Information gathered from transmitted light microscopy was used as the basis for electron microprobe (EMP) analysis using a JEOL JXA8230 electron microprobe located at AGH University of Science and Technology, Kraków, Poland. Back-scattered electron (BSE) images were acquired with both high-brightness/low-contrast and low-brightness/high-contrast settings, the latter utilized specifically to image garnet, zircon, and monazite to observe chemical zoning of the minerals. Semi-quantitative wavelength-dispersive spectroscopy (WDS) major element chemical maps of Ca, Fe, Mg, Mn, and Y were acquired for one representative garnet grain in paragneiss SM19-03. The map was acquired with a beam diameter of 4 μm, an accelerating voltage of 15 keV and beam current of 100 nA with a dwell time of 100 ms. The map was coupled with a WDS profile of garnet, acquiring quantitative data for Na_2O, SiO_2, Al_2O_3, MgO, K_2O, CaO, TiO_2, FeO, MnO, and Cr_2O_3. The quantitative WDS analyses were acquired using a 1 μm beam diameter, an accelerating voltage of 15 keV, and a beam current of 20 nA. The following natural minerals and synthetic standards were used for calibration: albite (Si, Al, Na), diopside (Ca, Mg), sanidine (K), rutile (Ti), fayalite (Fe), rhodonite (Mn), and Cr_2O_3 (Cr). Reflective light (RL) images were obtained of all zircons and monazites that were selected for geochronology and trace element analysis.

Zircon and monazite (Th-)U–Pb geochronology and trace element analysis

Zircon and monazite grains were analyzed in situ within standard 30 μm polished thin sections. The BSE and RL images of the grains were used to select the locations for (Th-)U–Pb geochronology and trace element analysis. Locations were selected to analyze different chemical domains within the zircon or monazite grains and also to avoid fractures, inclusions, domain boundaries, and grain edges. The geochronology and trace element analyses were conducted during four sessions (two for zircon and two for monazite) at the at the Vegacenter, Swedish Museum of Natural History (Stockholm, Sweden). Geochronology was conducted using an ESI NWR193 ArF excimer laser ablation system and a Nu Plasma II multi-collector inductively coupled plasma mass spectrometer (MC-ICP-MS). The m/z (mass-to-charge ratios) corresponding to masses 202, 204, 206, 207 and 208 were measured on ion counters and those corresponding to 232, 235 and 238 were measured on Faraday collectors. For zircon, a beam diameter of 15 μm was used for ablation at a frequency of 7 Hz and laser fluence of 2.0 J/cm^2. For monazite, a beam diameter of 6 μm was used for ablation at a frequency of 5 Hz and laser fluence of 2.7 J/cm^2. Helium

was used as a sample carrier gas (flow rate of 0.45 L/min for zircon and 0.35 L/min for monazite), which was then mixed with Argon (mixed gas flow rate of 0.80 L/min for zircon and 0.62 L/min for monazite). The data collection procedures included a 20 s ablation time, a 20 s washout time, and a 0.5 s integration time. The data for both zircon and monazite were processed using the Iolite add-on 'VizualAge' data reduction scheme (v. 2.5; Petrus and Kamber, 2012).

The zircon trace element (REE) and monazite trace element (Sr, Y, REE) data were collected during subsequent sessions using an Attom high-resolution inductively-coupled plasma mass spectrometer (HR-ICP-MS) and the same ESI NWR193 ArF excimer laser ablation system that was used for geochronology. For zircon, the laser was operated with a beam diameter of 15 μm at a frequency of 8 Hz and laser fluence of 4.2 J/cm^2. For monazite, the laser was operated with a beam diameter of 6 μm at a frequency of 5 Hz and laser fluence of 2.7 J/cm^2. Helium was used as a sample carrier gas (flow rate of 0.55 L/min for zircon and 0.35 L/min for monazite), which was then mixed with Argon (mixed gas flow rate of 0.84 L/min for zircon and 0.83 L/min for monazite). The data for both zircon and monazite were processed using an in-house Excel spreadsheet.

For both U–Pb geochronology and REE analysis, '91500' zircons (c. 1065 Ma; Wiedenbeck et al. 2004) were used as the primary reference material and 'GJ-1' (c. 609 Ma; Jackson et al. 2004), 'Plešovice' (c. 337 Ma; Sláma et al. 2008) and Temora-2 zircons (c. 417 Ma; Black et al. 2004) were used as secondary reference materials. For monazite Th–U–Pb geochronology, '44069' monazites (424.9 ± 0.4 Ma; Aleinikoff et al. 2006) were used as the primary reference material and 'Manangotry' (555 ± 2 Ma; Paquette and Tiepolo, 2007) and 'Skalna' (c. 311 Ma; Szopa et al. 2017) monazites were used as secondary reference materials. For monazite trace element analysis, 'Moacyr' monazites were used as the primary reference material with Y and REE values provided by the University of California, Santa Barbara LASS-ICP-MS laboratory. The '44069' and 'Manangotry' monazites were used as the secondary reference materials for Y and REE. The Sr values were normalized to the concentrations in '44069' monazites reported by Holder et al. (2015).

After geochronological and trace element analyses, a second set of RL images of all grains were obtained to show the exact locations of the ablation pits for each zircon and monazite grain. Due to the small sizes of some grains/domains, the new RL images were overlaid on the BSE images to identify ablations that overlapped with grain edges, fractures, inclusions, or that potentially mixed different chemical zones. The resulting datasets were also scrutinized for outliers and were compared with the locations of ablation pits, the combination of which was used as the basis to accept or reject each individual analysis. No blanket criteria were

used to filter entire datasets (e.g., discordance cutoffs) to prevent discarding individual data points that are outliers due to geological processes (e.g., Pb-loss). Concordia plots of the accepted analyses were constructed using IsoplotR (v. 4.1) with the default decay constants and $^{238}U/^{235}U$ value (Vermeesch, 2018). The reported error correlations (rho) for $^{207}Pb/^{235}U$ and $^{206}Pb/^{238}U$ were used for the Wetherill concordia (for zircon) and Th–U–Pb concordia (for monazite; Vermeesch, 2020) diagrams. Error correlations between other ratios were not used to create the Th–U–Pb concordia diagrams of the monazite geochronological data. All uncertainties are reported at the 2σ level. Rare earth element plots were created according to McDonough and Sun (1995).

Results

Petrography of the Sippmikk paragneiss

The two samples of the Sippmikk paragneiss (SM19-02 and SM19-03) are predominantly composed of quartz, plagioclase, biotite, white mica, garnet, and kyanite with lesser volumes of K-feldspar, zircon, monazite, allanite, apatite, clinozoisite, rutile, magnetite, pyrite, and carbonate (Figs. 2, 3, 4, 5). The rock foliations are defined both by alignment of minerals (i.e., white mica, biotite, and quartz ribbons) as well as sub-mm compositional layering consisting of quartzofeldspathic and micaceous domains. The quartzofeldspathic domains are dominated by fine-grain plagioclase and quartz grains (< 200 μm diameter). Quartz grains show undulous extinction and evidence of subgrain development. Thin layers of fine grain biotite and white mica (< 150 μm length) are found throughout the plagioclase and quartz matrix. The micaceous domains are dominated by white mica porphyroblasts (0.5–4.5 mm length) with finer biotite (0.1–1 mm length) and minor plagioclase and quartz grains (Fig. 2A). Pockets of coarse-grain biotite (0.2–1.5 mm length of individual grains) are found locally within the paragneiss (Fig. 2B). Porphyroblasts of plagioclase (1–5 mm diameter), subhedral to euhedral garnet (1–2.5 mm diameter), and kyanite (100–250 μm length) are found within both domains. Plagioclase often contain lobate and ovoid quartz intergrowths (Fig. 2C). Two morphologies of kyanite can be observed, the first with quartz intergrowths similar to plagioclase, and the second without intergrowths or abundant inclusions. The grain boundaries of the second type terminate against garnet or matrix quartz (Fig. 2D).

Many of the garnet grains in the Sippmikk paragneiss exhibited three zones in BSE intensity: (1) a dark core, (2) a bright mantle, and (3) a dark rim (Fig. 3). The boundaries between the cores and mantles are indistinct and curvilinear, whereas the boundary between the mantles and rims are much more definitive, as best observed
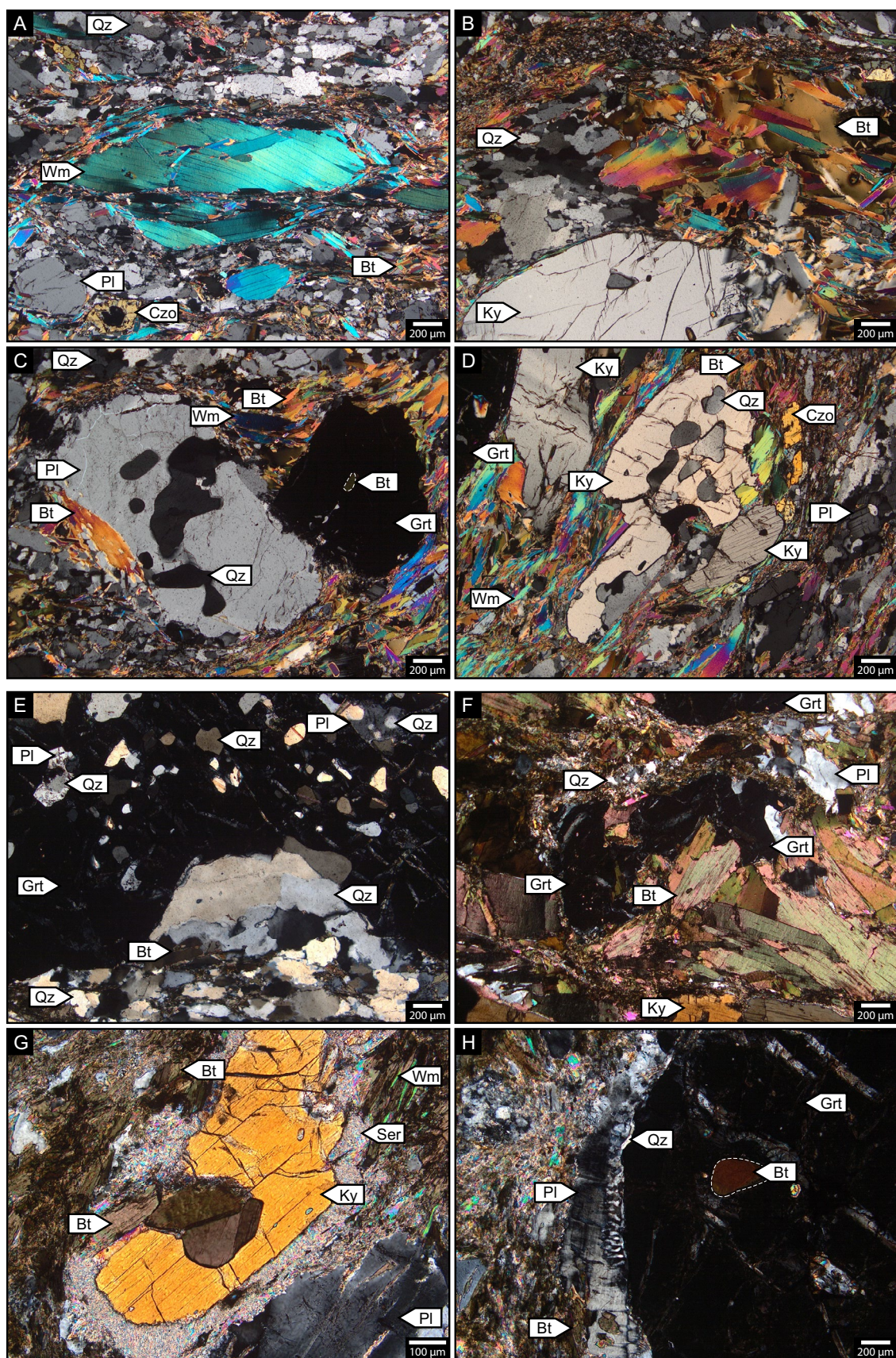
◀**Fig. 2** Cross-polarized transmitted light microphotographs showing textural features related to partial melting in the Sippmikk paragneiss (**A**–**D**) and the Kittelfjäll paragneiss (**E**–**H**). **A** White mica porphyroblasts with undulous extinction surrounded by smaller, recrystallized white mica grains. The matrix consists of recrystallized quartz, plagioclase porphyroblasts, fine-grain biotite, and clinozoisite. **B** A pocket of coarse-grain biotite and recrystallized quartz adjacent to a kyanite porphyroblast within the fine-grain matrix. **C** Plagioclase porphyroblast with lobate and ovoid quartz intergrowths adjacent to a garnet porphyroblast containing a rounded biotite inclusion. The porphyroblasts are surrounded by fine-grain white mica, biotite, and recrystallized quartz constituting the matrix. **D** Kyanite porphyroblasts showing different morphological characteristics. The kyanite in the center contains lobate and ovoid quartz intergrowths whereas the other kyanite porphyroblasts do not show intergrowths and their grain abruptly boundaries terminate against garnet (top left) or again recrystallized quartz (lower right). **E** Poikiloblastic garnet within the quartzofeldspathic domain of the paragneiss. The garnet contains lobate and ovoid quartz inclusions as well as inclusions of quartz surrounded by plagioclase (top left and right). The lower half of the microphotograph shows the boundary of the garnet porphyroblast embayed by coarse-grain quartz adjacent to fine-grain recrystallized quartz with biotite that define the foliated rock matrix. **F** Irregularly shaped garnet porphyroblasts surrounded and embayed by coarse-grain biotite within the biotite-kyanite domain of the paragneiss. The coarse-grain biotite is associated with plagioclase and fine-grain quartz. **G** Kyanite porphyroblast within the biotite-kyanite domain of the paragneiss. The kyanite is partially pseudomorphed by sericite and intergrown with coarse-grain biotite, collectively surrounded by a fine-grain matrix of biotite, white mica, and quartz. **H** Garnet porphyroblast with a round biotite inclusion within the biotite-kyanite domain of the paragneiss. Locally, the garnet boundary has a thin film of quartz in contact with plagioclase, exhibiting myrmekite texture. The matrix is characterized by fine-grain biotite, plagioclase, quartz, white mica, and sericite. A plagioclase porphyroblast is also adjacent to the kyanite. Minerals are abbreviated according to Whitney and Evans (2010)

with Ca and Mn chemical maps (Fig. 3A). Additionally, some garnet grains exhibited only a BSE bright interior surrounded by a dark exterior, reflecting the mantle-rim zones of the garnet. One representative garnet grain showing all three zones was selected for a quantitative major element chemical profile across all three zones together with semi-quantitative chemical maps (Ca, Fe, Mg, Mn, Y; Fig. 3A). The results show that the cores are defined by an endmember composition of $Alm_{63-61}Py_{23-20}Grs_{13-11}Sps_{5-4}$, the mantles by $Alm_{67-64}Py_{19-18}Grs_{11-8}Sps_{7-5}$, and the rims by $Alm_{67-63}Py_{20-18}Grs_{18-14}Sps_{1-0}$ (Table S1). The chemical maps of the garnet illustrate the chemical variations between the three zones that correspond to the BSE intensities (compare Fig. 3A with Fig. 3B, C).

Inclusions in garnets in all paragneiss samples were characterized with BSE imaging. For the Sippmikk paragneiss garnet, inclusions of biotite, white mica, albite, quartz, zircon, and magnetite are found in all three zones (Figs. 3, 4, 5). Most notably, polymineralic inclusions containing these minerals with negative garnet crystal shapes are abundant in the BSE bright zones (Fig. 3). Biotite can be found throughout garnet zones and are often

subrounded in shape (Figs. 2C, 4E). Kyanite inclusions are also found in the BSE bright garnet. Rutile inclusions are only found within the BSE dark rims (Fig. 3). No Ti-bearing phases (i.e., ilmenite nor titanite) are found within the BSE dark cores or bright mantles. The garnet porphyroblasts are locally embayed by coarse-grain polycrystalline quartz.

Petrography of the Kittelfjäll paragneiss

The Kittelfjäll paragneiss (MJ18-05A) is composed of quartz, K-feldspar, plagioclase, biotite, garnet, kyanite, and white mica with accessory sericite, rutile, ilmenite, zircon, monazite, apatite, allanite, clinozoisite, pyrite, and carbonate (Figs. 2, 3, 6). The foliation of the paragneiss is defined by alignment of minerals (i.e., biotite, kyanite, and quartz ribbons) and cm-scale compositional layering consisting of quartzofeldspathic and biotite-kyanite domains. The quartzofeldspathic domains are defined by large plagioclase porphyroblasts (1–4 mm diameter) within a matrix of smaller plagioclase, K-feldspar, and quartz grains (< 300 μm diameter), the latter often defining ribbons (< 1.5 mm length). Thin, discontinuous layers of fine grain biotites (< 100 μm length) are common within the quartzofeldspathic domain. The biotite-kyanite domain is dominated by fine (< 100 μm) to coarse biotite grains (up to 1.5 mm length), kyanite porphyroblasts (1–3 mm length), and subordinate white mica, plagioclase and quartz (Fig. 2F, G). Some of the kyanite grains are intergrown with coarse-grain biotite (Fig. 2G). Both kyanite and plagioclase grains within these domains are surrounded by distinct regions of sericite (< 100 μm thick) that follow the grain shapes. Garnet porphyroblasts are found throughout the paragneiss but are more abundant within the biotite-kyanite domains. (Fig. 2H). Within that domain, garnet grains often have irregular shapes and inundated by coarse biotite (Fig. 2F) and are locally surrounded by thin films of quartz with a myrmekitic contact with plagioclase (Fig. 2H).

The garnet porphyroblasts typically show subhedral crystal habits with a low-density of inclusions. However, two instances of anhedral poikiloblastic garnet with abundant, coarse inclusions of quartz and quartz surrounded by plagioclase (< 200 μm diameter) are also present within the quartzofeldspathic domain (Fig. 2E). These garnet porphyroblasts also have embayments of coarse-grain polycrystalline quartz. The subhedral garnets contain inclusions of quartz, rutile, biotite, white mica, zircon, and monazite (Fig. 6E, F). Similar to the Sippmikk paragneisses, some garnet grains also contain polymineralic inclusions with negative garnet crystal shapes (Fig. 3G) and subrounded biotite inclusions (Fig. 2F). High-contrast BSE images showed no zoning of any garnet porphyroblasts, in accordance with the results of Bukała et al. (2020b). The lack of identifiable garnet zoning
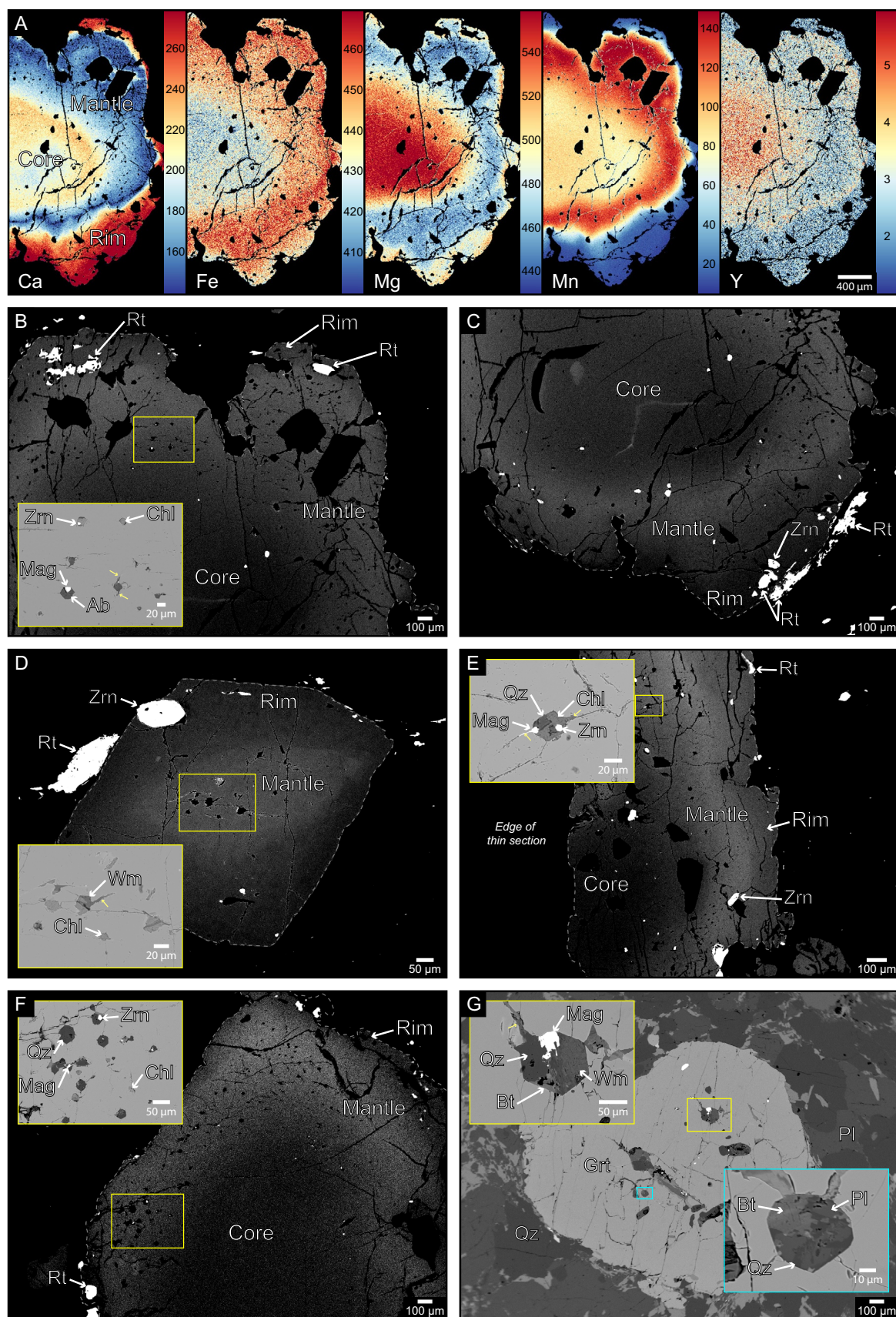
◄**Fig. 3** BSE images displaying Sippmikk and Kittelfjäll paragneiss garnet and their inclusions. **A** Electron microprobe semi-quantitative chemical maps of a representative garnet from Sippmikk paragneiss sample SM19-03. Colored scale bars present the element counts for the respective maps to the left. **B–F**: High-contrast BSE images of garnet grains in Sippmikk paragneiss samples SM19-03 (**B–E**) and SM19-02 (**F**). The garnet in BSE images **B** and **C** is the same garnet presented in the chemical maps. The external boundaries of garnets in all BSE images are traced by the dashed grey line and the garnet zones are annotated as core, mantle, and rim. Zircon grains with metamorphic rims and rutile grains are indicated, showing their positions with respect to the garnet zones. The insets in for each BSE image present a low-contrast BSE image of melt inclusions present in the BSE bright garnet zones. **G**: Low-contrast BSE image of a garnet in the Kittelfjäll paragneiss sample MJ18-05A. Melt inclusions are highlighted in the inset BSE images. White arrows in the insets highlight decrepitation cracks. Minerals are abbreviated according to Whitney and Evans (2010)

prevents classification of inclusions within specific growth zones of the garnet.

Zircon U–Pb geochronology

Zircon grains in the Sippmikk paragneiss of the Avardo Gneiss (sample SM19-03) are found amongst the matrix minerals and as inclusions in both garnet and kyanite porphyroblasts. Many large zircon grains exhibit a core-rim texture with BSE bright cores that are chemically heterogeneous, commonly with oscillatory zoning patterns, and BSE dark rims that are relatively chemically homogeneous. Zircon grains with these characteristics are only found within garnet mantles, rims, in kyanite, and predominantly in micaceous domains of the paragneiss matrix (Figs. 3, 4). A thinner, brighter outer rim is observed on some of the grains, but they were not analyzed as they are thinner than the 15 μm beam diameter used for analysis.

A total of thirty-six trace element analyses and forty-seven geochronological analyses were accepted from forty-four zircon grains. The analyses were accepted following the protocol outlined in the methodology. The results are summarized in Table 1 and presented in full in Tables S2 and S3. Fourteen trace element analyses of the zircon cores yielded steep chondrite normalized HREE patterns, whereas twenty-two analyses of rims produced significantly shallower HREE patterns (Fig. 7A; Table 1). LREE were typically below the detection limit for the zircon grains but nine analyses of the cores show more pronounced negative Eu anomalies than four analyses of the rims (Fig. 7A; Table 1). Thirty-two geochronological analyses of zircon cores provide a range of $^{207}Pb/^{235}U$ dates from 661.7 ± 13.6 Ma to 1736.4 ± 35.3 Ma, and $^{206}Pb/^{238}U$ dates from 639.9 ± 15.3 Ma to 1712.9 ± 33.9 Ma with discordance values ranging from -26.4 to 0.6% (with negative values representing normal discordance). In Wetherill concordia space, the analyses plot as broad discordia line

(Fig. 7B). Model-I linear regression of analyses with > 4% normal discordance (n: 21) provides a lower-intercept of 487.5 ± 90.7 Ma (MSWD: 14). Fifteen U–Pb analyses of rims provide $^{207}Pb/^{235}U$ dates from 469.5 ± 13.1 Ma to 501.1 ± 10.8 Ma, and $^{206}Pb/^{238}U$ dates from 470.9 ± 11.5 Ma to 494.2 ± 12.1 Ma with discordance ranging between -2.5 to 2.0% (Fig. 7B). A Wetherill concordia age for these analyses is calculated to 482.5 ± 3.7 Ma (MSWD: 1.9). The zircon cores are generally higher in U content compared to the rims (Table 1).

Monazite Th–U–Pb geochronology

Monazites were analyzed from two samples of the Sippmikk paragneiss of the Avardo Gneiss (samples SM19-02 and SM19-03). The results are summarized in Table 1 and presented in full in Tables S4 and S5. Monazites in paragneiss SM19-02 are found in the BSE dark garnet rims and in the matrix, whereas monazites in paragneiss SM19-03 are only found within the matrix (Fig. 5). The matrix monazites in both rocks are associated with mica-rich regions. All monazite grains are surrounded by mineral agglomerations consisting of apatite, allanite, clinozoisite and other REE-bearing phases. BSE images of monazites demonstrate no obvious chemical zoning (Fig. 5).

For paragneiss SM19-02, a total of twenty geochronological analyses and seventeen trace element analyses were accepted from ten monazite grains. For paragneiss SM19-03, twelve geochronological analyses and ten trace element analyses were accepted from four grains. The analyses were accepted according to the protocol outlined in the methodology. The REE, Y, and Sr content of monazites in both paragneisses are similar (Table 1) and no systematic trends are recognized for either sample. Monazite in paragneiss SM19-02 show higher Th/U values than monazite in paragneiss SM19-03, which overall decrease with younger $^{208}Pb/^{232}Th$ dates (Fig. 8A; Table 1). Monazite in paragneiss SM19-02 yielded a spread of concordant dates with $^{208}Pb/^{232}Th$ dates ranging from c. 412.5 to 456.9 Ma, whereas the results from paragneiss SM19-03 cluster on concordia, producing an age of 420.6 ± 2.0 Ma (MSWD: 1.2; Fig. 8B).

Monazites were analyzed from one sample of the Kittelfjäll paragneiss of the Marsfjället Gneiss (sample MJ18-05A; Tables S4 and S5), which was obtained from the same rock sample that Bukała et al. (2020b) used to conduct zircon geochronology. The results are summarized in Table 1 and presented in full in Tables S4 and S5. In the paragneiss, monazite grains are predominantly found in the biotite-kyanite domain, but are also found to be associated with smaller biotite pockets in the quartzofeldspathic domains and also included in garnet and kyanite. Regardless of the textural position, the BSE images of the monazite reveal three domains (Fig. 6): (1) BSE-dark, homogeneous
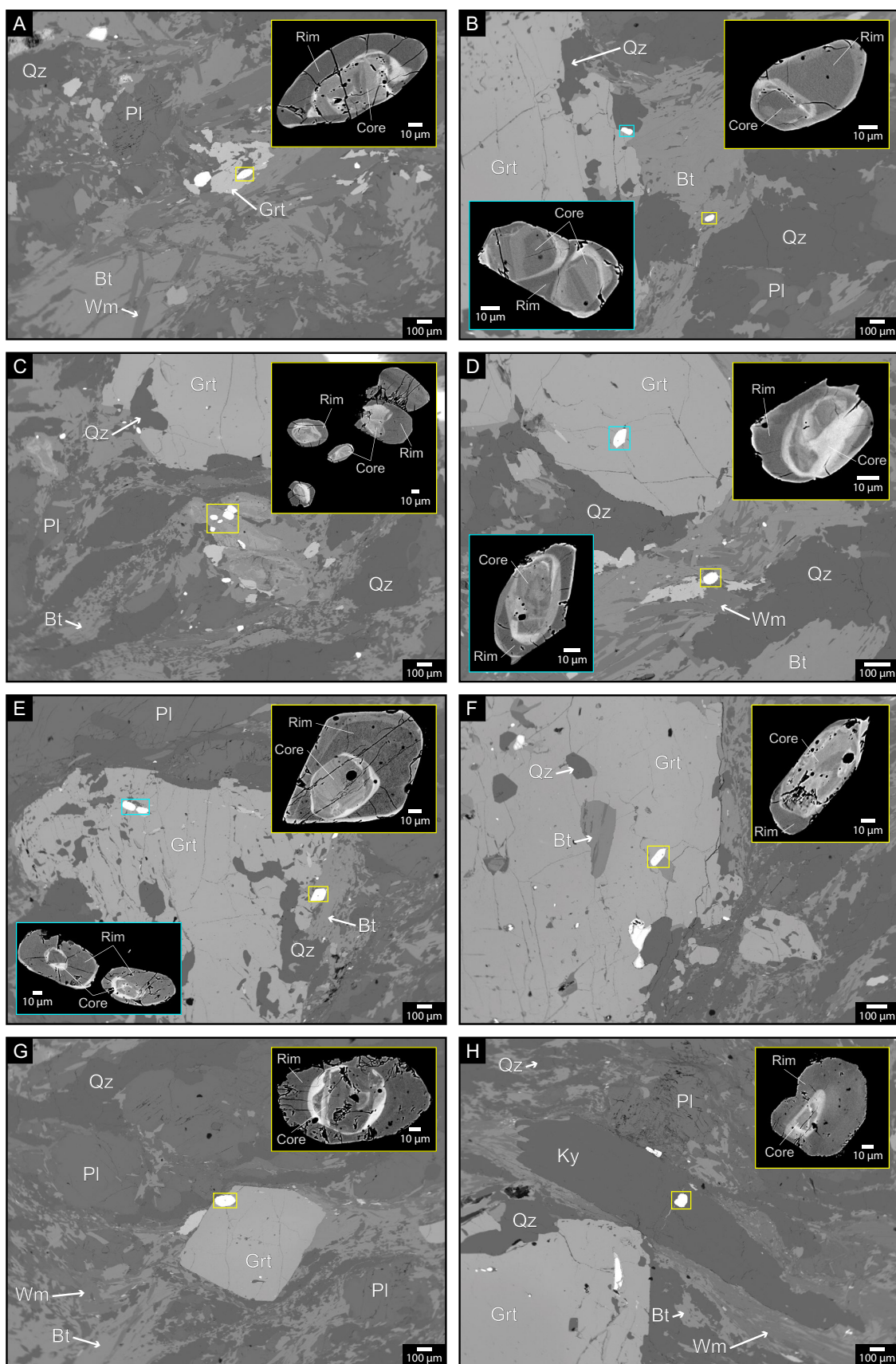
◀**Fig. 4** BSE images showing the general mineral assemblages of Sippmikk paragneiss sample SM19-03 and highlighting the textural positions of zircons that were analyzed. High-contrast BSE image insets exhibit the zircon core-rim zonation. **A–E**: Zircon grains located in the paragneiss matrix close to garnet porphyroblasts. **D–G**: Zircon grains included in garnet porphyroblasts. **H**: A zircon grain included in a kyanite porphyroblast. The low-contrast BSE images F and G correspond to the high-contrast BSE images in Fig. 2F and E, respectively. Minerals are abbreviated according to Whitney and Evans (2010)

to weakly zoned cores, (2) BSE-medium, heterogeneously zones mantles, and (3) BSE-bright, homogeneous rims. The boundaries between all three domains are irregular, often curvilinear or sharp and angular. In some grains, the mantles appear to be transected by the rims, and the cores transected by both mantles and rims.

A total of sixty trace element analyses and eighty-one geochronological analyses were accepted from thirty-three monazite grains in the Kittelfjäll paragneiss. The analyses were accepted based on the protocol outlined in the methodology. The grains are located in the matrix, in garnet, or in kyanite, but no systematic patterns were recognized according to the textural positions. All three monazite domains were analyzed, and where possible, Th–U–Pb analyses were conducted in the same domains as the trace element analyses. The Th/U ratios of the monazite show a weak correlation with Th content and a strong correlation with U content (Fig. 9A). Fifteen trace element analyses of the monazite cores show distinctly lower Th/U with significantly higher U, Y, HREE, weakly elevated Sr content, and subdued negative Eu anomalies (Eu*) compared to thirty analyses of mantles and fifteen analyses of rims. The mantles and rims are chemically indistinguishable (Fig. 9A, B; Table 1). Seventeen geochronological analyses of the cores cluster in $^{208}Pb/^{232}Th$ vs. $^{206}Pb/^{238}U$ concordia space, providing an age of 481.6 ± 2.1 Ma (MSWD: 2.0; Fig. 9C). Forty geochronological analyses of the mantles and twenty-four analyses of rims produced indistinguishable results in concordia space and range from c. 493 to 455 Ma with an average concordia age of 476.6 ± 1.5 Ma (MSWD: 4.3; Fig. 9D). To delimit the endmember ages of the collective mantle and rim results, the ten oldest and ten youngest analyses were used to calculate ages, yielding 488.9 ± 1.9 Ma (MSWD: 0.8) and 463.1 ± 1.8 Ma (MSWD: 1.1), respectively.

Discussion

Metamorphic Evolution of the Avardo Gneiss at Sippmikk Creek

The Avardo Gneiss has previously been described to have undergone partial melting that was responsible for development of compositional layering of the parag-neisses (Van Roermund and Bakker 1983). The Sippmikk paragneiss (belonging to the Avardo Gneiss) exhibits layering akin to partial melting. The matrix phases of the parag-neiss show evidence of recrystallization (Fig. 2), thereby preventing unequivocal identification of melt-related microstructures throughout the rock volumes. However, the polyphase inclusions with decrepitation cracks that are found within the Sippmikk paragneiss garnet mantles are interpreted as melt inclusions, indicating that garnet is peritectic (Fig. 3; Cesare et al. 2009; Ferrero et al. 2012, 2015; Bartoli et al. 2013). The subrounded biotite inclusions in garnet (Fig. 2C, H) and the coarse-grain quartz embayments are further evidence for peritectic garnet growth, attributed to biotite dehydration melting (Braun et al. 1996; Fitzsimons 1996; Waters 2001; Barbey 2007).

There is evidence for white mica-dehydration melting within the kyanite stability field prior to biotite-dehydration melting. The peritectic garnet mantles in the Sippmikk par-agneiss envelope garnet cores with bell-shaped Y zoning. This zoning indicates the cores formed during prograde metamorphism with Y preferentially partitioned to garnet according to Rayleigh fractionation (Symmes and Ferry 1992; Lanzirotti 1995; Pyle and Spear 2003). The irregular and curvilinear boundaries between the cores and mantles, together with the high Mn content of the latter (Fig. 3A–F), suggests that the garnet cores were partially resorbed (Perchuk et al. 2005, 2008; Liu et al. 2014; Xia et al. 2016; Xia and Zhou 2017). Garnet has been documented to be a reactant during white mica-dehydration melting, producing kyanite and biotite as products (Indares and Dunning 2001; Lang and Gilotti 2007). Thus, the kyanite and biotite inclusions within the garnet mantles may be products of the melting prior to peritectic garnet growth. Furthermore, the kyanite porphyroblasts intergrown with lobate quartz can be of peritectic origin.

Zircon with core-rim structure occur within the garnet mantles, rims and matrix. The zircon structures are interpreted as xenocrystic cores that are overgrown by metamorphic rims (Fig. 4; e.g., Whitehouse and Platt 2003). The xenocrystic cores provide a dispersion of dates and typical igneous REE patterns that is representative of a detrital zircon provenance. The discordance of the core U–Pb dates, producing a lower intercept of 487.5 ± 90.7 Ma (Fig. 7B), demonstrates Pb-mobilization broadly coeval with Caledonian tectonism, requiring high temperature or dissolution-reprecipitation in order to mobilize Pb (Cherniak and Watson 2001; Harley et al. 2007; Rubatto 2017). The shallow HREE slopes of the zircon rims, compared to the zircon cores (Fig. 7A), is a typical pattern for metamorphic zircon that formed either after or coeval with garnet crystallization in a closed system environment (Rubatto 2002; Hermann and Rubatto
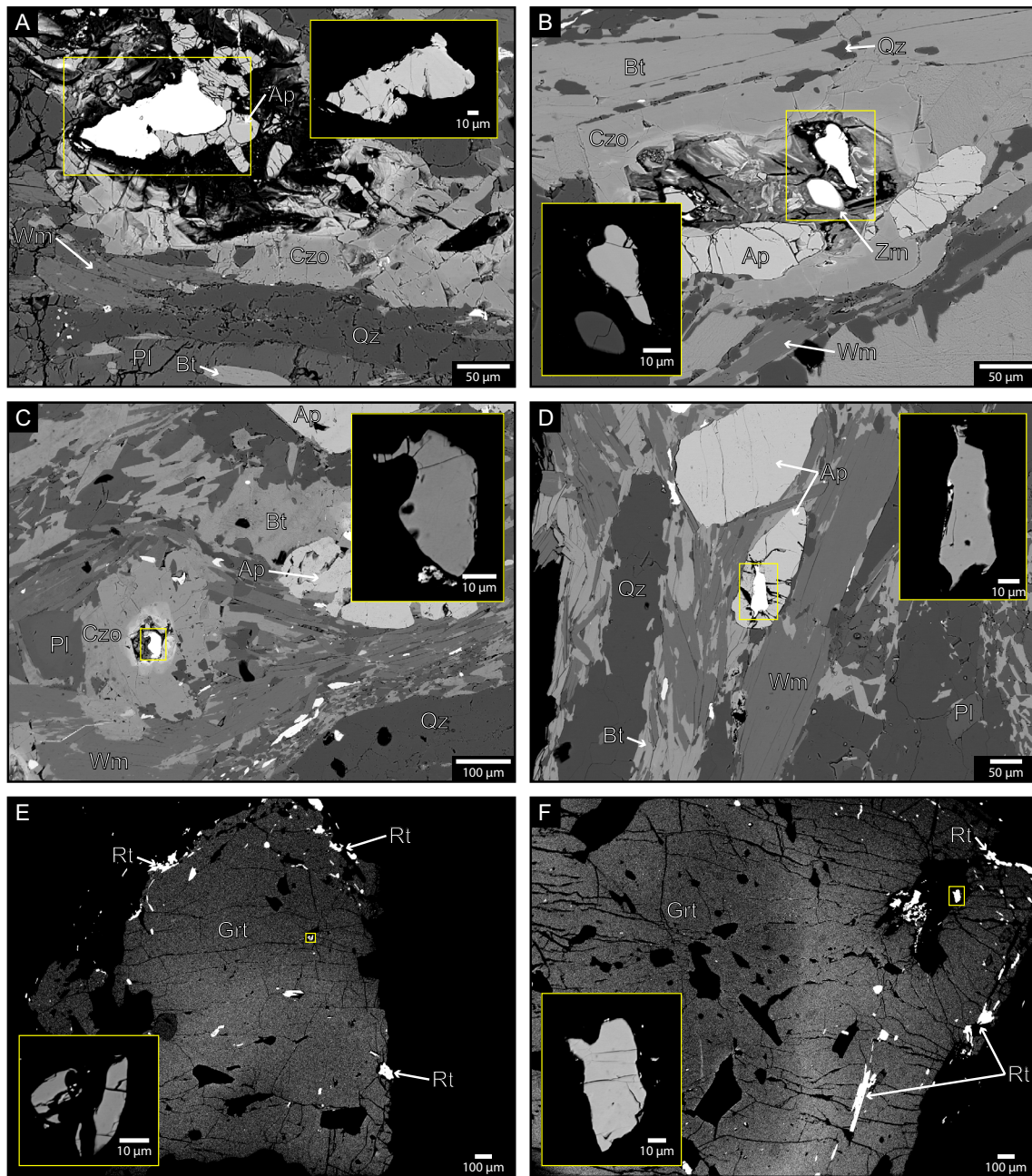
Fig. 5 BSE images showing the general mineral assemblages of Sipp-mikk paragneiss samples and highlighting the textural positions of monazite that were analyzed. High-contrast BSE image insets illustrate the chemical homogeneity of the monazite grains. **A–B**: Monazite in the matrix of sample SM19-03. **C–D**: Monazite in the matrix of sample SM19-02. **E–F**: High-contrast BSE images of garnet in sample SM19-02, demonstrating the locations of monazite within the BSE dark garnet rims, spatially associated with rutile. Minerals are abbreviated according to Whitney and Evans (2010)

2003; Whitehouse and Platt 2003; Hokada and Harley 2004). Considering that resorption of garnet cores would release HREE into the reactive bulk rock, the zircon rims are best explained to have formed coeval with peritectic garnet during biotite-dehydration melting. The subdued Eu anomalies of the rims suggest melting may have occurred in (U)HP conditions. This evolution would explain the

inclusions of rounded biotite, kyanite, and zircon in peritectic garnet. This would also infer that the zircon rims formed after kyanite, yet they are found within kyanite porphyroblasts. However, the kyanite morphologies within the matrix (Fig. 2D) suggest two generations, which was described for the Avardo Gneiss by Van Roermund and Bakker (1983). The first generation of kyanite was
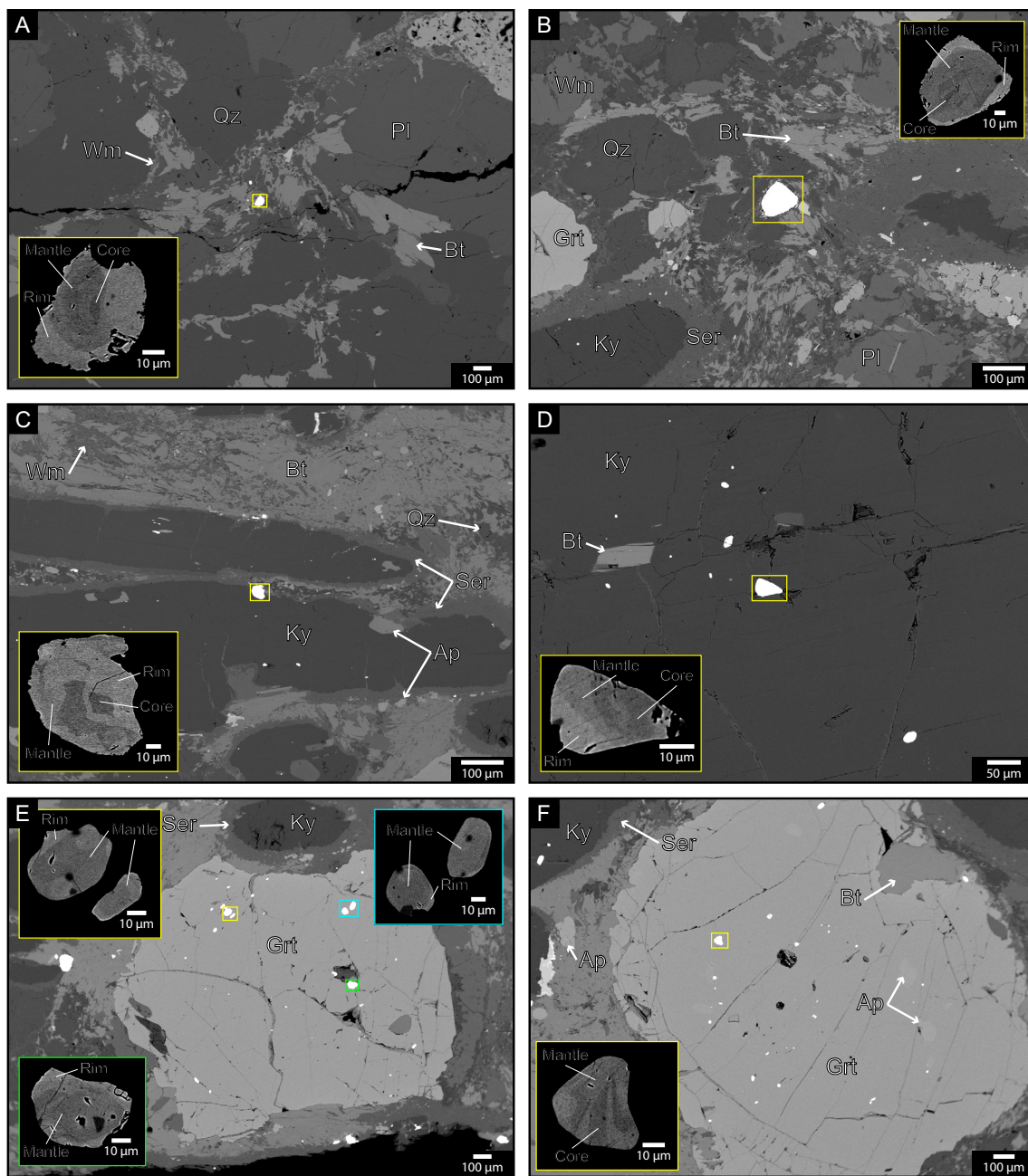
Fig. 6 BSE images showing the general mineral assemblages of Kittelfjäll paragneiss sample MJ18-05A and highlighting the textural positions of monazites that were analyzed. High-contrast BSE image insets demonstrate the core-mantle-rim chemical zoning of the monazite grains. **A–B**: Monazites in the paragneiss matrix. **C–D**: Monazites included in kyanite porphyroblasts. **E–F**: Monazites included in garnet porphyroblasts. Minerals are abbreviated according to Whitney and Evans (2010)

reported to occur with K-feldspar, in line with white mica-dehydration melting. The second generation was reported to overgrow sillimanite (not observed in the studied paragneisses) and occur in relation with staurolite, perhaps reflecting Middle Ordovician metamorphism (Brueckner and Van Roermund 2007).

Monazites in paragneiss SM19-03 provide a more concise cluster of dates and Th/U values, providing definitive evidence of the late Silurian event at 420.6 ± 2.0 Ma (Fig. 8B), reproducing previous geochronology suggesting partial melting of the Avardo Gneiss at 423 ± 5 Ma (Williams and Claesson 1987). However, there is no obvious textural evidence in the Sippmikk paragneiss to suggest partial melting associated with monazite formation. The monazite in paragneiss SM19-02 are found both within garnet rims and in the matrix. The spread of

Table 1 Geochronology and trace element summary

	SM19-03 Zrn-Core	SM19-03 Zrn-Rim	SM19-02 Mnz	SM19-03 Mnz	MJ18-05A Mnz-Core	MJ18-05A Mnz-Mantle	MJ18-05A Mnz-Rim
Trace element analyses (#)	14	22	17	10	15	30	15
Eu*[1,2]	Min: 0.10 Max: 0.51 Avg.: 0.30	Min: 0.42 Max: 0.75 Avg.: 0.55	Min: 0.49 Max: 0.59 Avg.: 0.59	Min: 0.50 Max: 0.64 Avg.: 0.56	Min: 0.48 Max: 0.77 Avg.: 0.63	Min: 0.37 Max: 0.67 Avg.: 0.46	Min: 0.39 Max: 0.70 Avg.: 0.50
YbN/GdN[3]	Min: 11.8 Max: 67.5 Avg.: 31.0	Min: 1.4 Max: 16.3 Avg.: 7.4	Min: 12.9 Max: 34.8 Avg.: 21.6	Min: 13.4 Max: 25.4 Avg.: 19.6	Min: 33.2 Max: 376.7 Avg.: 111.5	Min: 143.0 Max: 787.4 Avg.: 427.6	Min: 184.7 Max: 572.7 Avg.: 309.3
Y (wt %)	–	–	Min: 0.79 Max: 1.62 Avg.: 1.11	Min: 1.08 Max: 1.68 Avg.: 1.35	Min: 0.55 Max: 1.34 Avg.: 0.95	Min: 0.10 Max: 0.74 Avg.: 0.32	Min: 0.09 Max: 0.72 Avg.: 0.27
Sr (ppm)	–	–	Min: 47 Max: 106 Avg.: 66	Min: 52 Max: 107 Avg.: 72	Min: 64 Max: 143 Avg.: 97	Min: 42 Max: 117 Avg.: 64	Min: 36 Max: 99 Avg.: 59
Geochronology analyses (#)	32	15	20	12	17	40	24
Discordance (%)[5]	–26.4 to 0.6	–2.5 to 2.0	3.4 to –3.3	1.7 to –3.8	2.3 to –1.0	2.2 to –2.5	2.3 to –2.4
U (wt %)	Min: 0.01 Max: 0.23 Avg.: 0.05	Min: 0.01 Max: 0.06 Avg.: 0.02	Min: 0.02 Max: 0.33 Avg.: 0.22	Min: 0.18 Max: 0.44 Avg.: 0.27	Min: 0.49 Max: 0.99 Avg.: 0.72	Min: 0.14 Max: 0.47 Avg.: 0.32	Min: 0.21 Max: 0.39 Avg.: 0.31
Th (wt %)	–	–	Min: 0.20 Max: 4.23 Avg.: 2.38	Min: 1.19 Max: 3.22 Avg.: 1.72	Min: 2.05 Max: 3.43 Avg.: 2.52	Min: 2.35 Max: 3.84 Avg.: 2.87	Min: 1.77 Max: 3.43 Avg.: 2.79
Th/U	–	–	Min: 7.5 Max: 14.7 Avg.: 10.7	Min: 4.6 Max: 9.7 Avg.: 6.4	Min: 2.6 Max: 5.4 Avg.: 3.6	Min: 6.2 Max: 18.8 Avg.: 9.7	Min: 6.0 Max: 12.9 Avg.: 9.2
Age (Ma)	487.5±90.7 MSWD: 14 (1-intercept)[4]	482.5±3.7 MSWD: 1.9 (concordia)	c. 412.5 to 456.9 ($^{208}Pb/^{232}Th$)	420.6±2.0 MSWD: 1.2 (concordia)	481.6±2.1 MSWD: 2.0 (concordia)	488.9±1.9[6] MSWD: 0.8 MSWD: 1.1 (concordia)	463.1±1.8[7]

[1] Eu anomaly (Eu*) is calculated as $EuN/\sqrt{(SmN \times GdN)}$

[2] Calculated using 9/14 and 4/22 analyses for zircon cores and rims, respectively

[3] Calculated using 17/22, 23/30, and 6/15 analyses for zircon rims, monazite rims, monazite mantles, and monazite rims, respectively

[4] 21/32 of the analyses were used to calculate the lower-intercept

[5] Calculated as $^{207}Pb/^{235}U$ vs. $^{206}Pb/^{238}U$ for zircon and $^{206}Pb/^{238}U$ vs. $^{208}Pb/^{232}Th$ for monazite

[6] Defined by 10 oldest dates of combined mantle/rim data

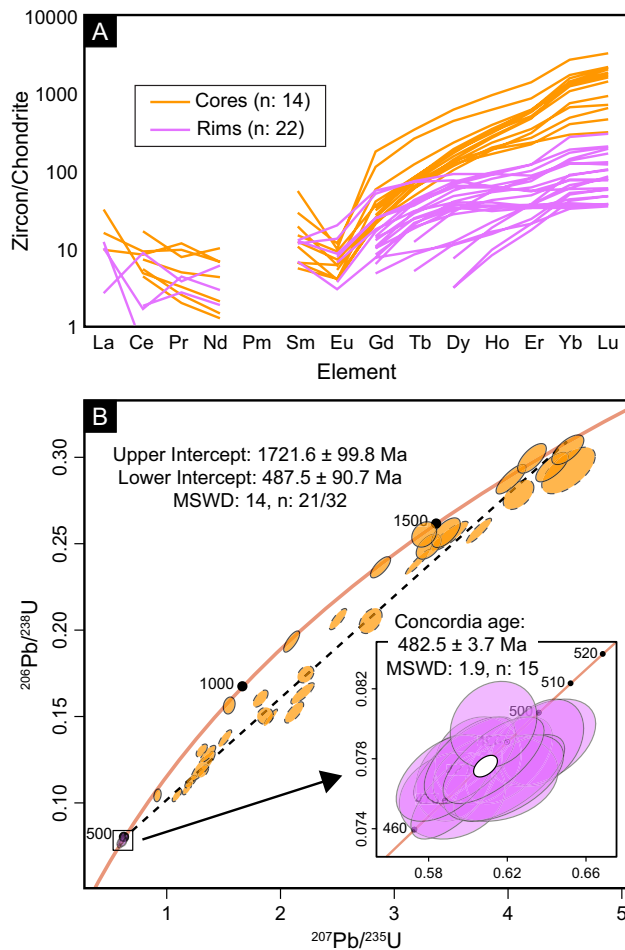[7] Defined by 10 youngest dates of combined mantle/rim data

Fig. 7 Results of zircon analyses for the Sippmikk paragneiss (sample SM19-03). **A** Results of zircon REE analysis for cores (orange lines) and rims (purple lines), normalized to chondrite REE values (McDonough and Sun 1995). **B** Wetherill concordia diagram showing the results of zircon geochronology. Orange ellipses show the results from the zircon cores whereas the purple ellipses show the results from the rims. The black dashed line represents a model-1 regression of the core analyses with > 4% normal discordance, denoted by the ellipses with dashed outlines. The inset of the Wetherill diagram highlights the rim analyses and the obtained concordia age, represented by the white ellipse

Fig. 8 Results of monazite analyses for the Sippmikk paragneiss (sample SM19-02 and -03). **A** Th/U ratios vs. $^{208}Pb/^{232}Th$ dates for the monazite analysis from both paragneiss samples. **B** Results of monazite geochronological analysis presented in $^{206}Pb/^{238}U$ vs. $^{208}Pb/^{232}Th$ concordia space. The concordia age for the analysis of sample SM19-03 is presented and represented by the white ellipse

Middle Ordovician to late Silurian dates that correlates with decreasing Th/U values (Fig. 8A) indicates that the monazites underwent dissolution-reprecipitation (Seydoux-Guillaume et al. 2003; Weinberg et al. 2020), which partially reset a Middle Ordovician (or older) history during a late Silurian metamorphic event (Fig. 10). As a result, it is possible that garnet rims formed during Middle Ordovician metamorphism and entrapped monazite (associated with staurolite and possibly second generation of kyanite; Van Roermund and Bakker 1983). The monazite then underwent dissolution-reprecipitation in late Silurian time, facilitated by fluid ingress along garnet fractures.
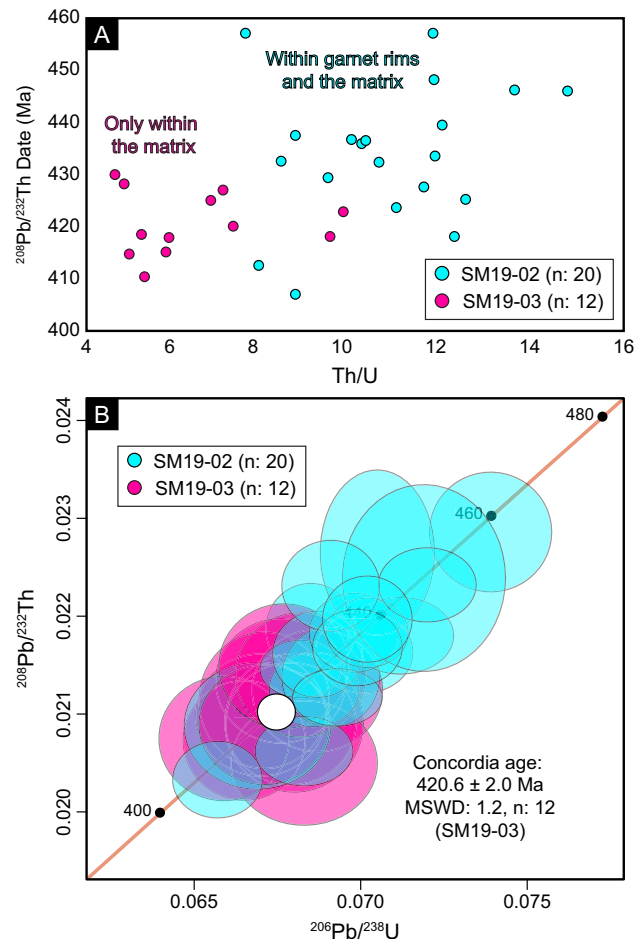
Metamorphic evolution of the Marsfjället Gneiss near Kittelfjäll

The compositional layering of the Kittelfjäll paragneiss is attributed to partial melting, resolved to late Cambrian/early Ordovician time (Bukała et al. 2020b). Similar to the Sippmikk paragneiss, the matrix of the Kittelfjäll paragneiss is recrystallized and partially retrogressed. However, the polymineralic inclusions (Fig. 3G), the embayed and poikiloblastic garnet (Fig. 2E), and subrounded biotite inclusions (Fig. 2H), all indicate biotite-dehydration melting of the paragneiss and peritectic garnet growth (Braun et al. 1996; Fitzsimons 1996; Waters 2001; Barbey 2007). Furthermore, many garnet grains are observed to be partially replaced by biotite (Fig. 2F) and are locally enveloped by quartz films in contact with plagioclase with myrmekitic texture (Fig. 2H). These features indicate garnet porphyroblasts
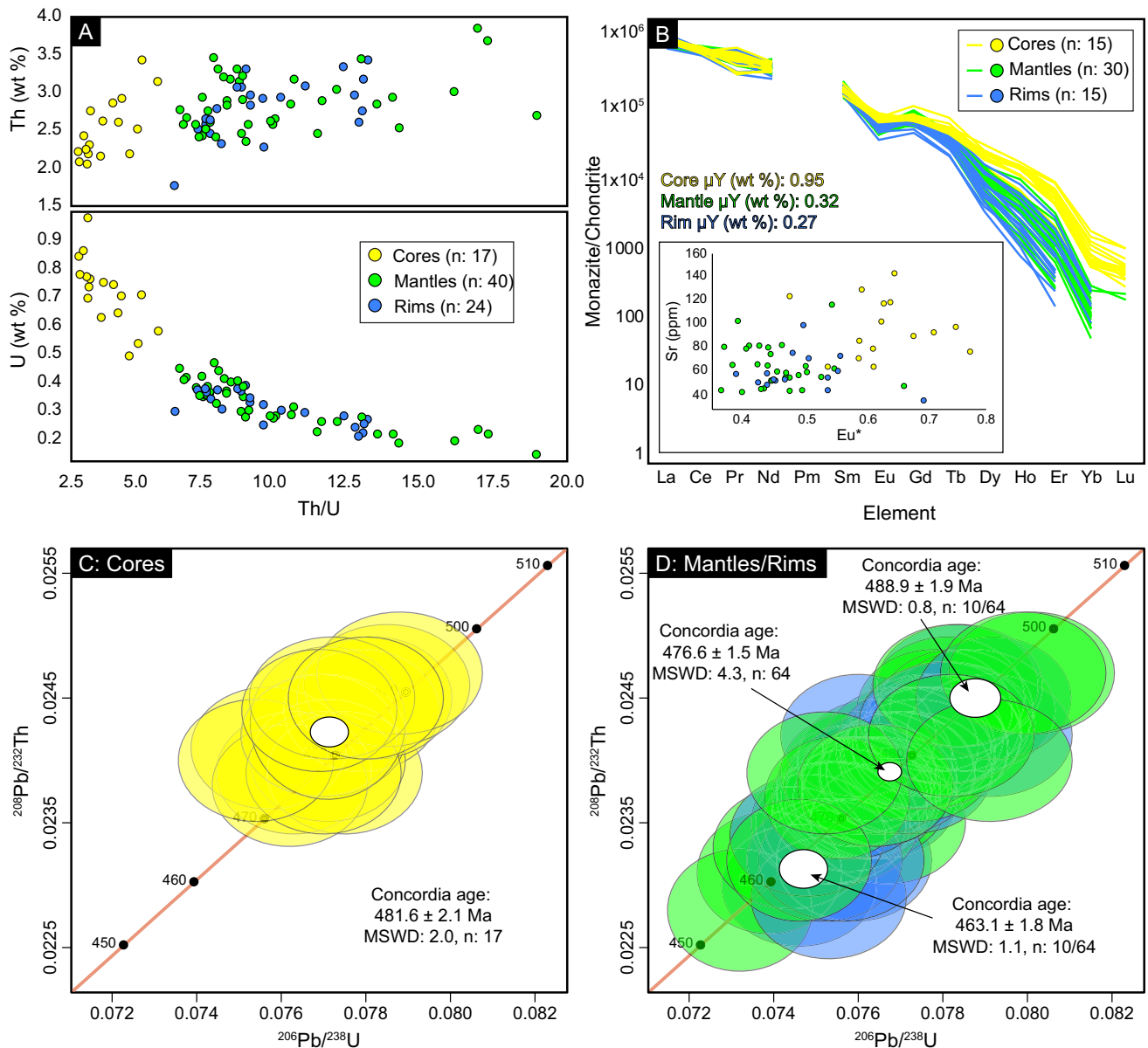
Fig. 9 **A** Th/U values vs. Th (wt %; top) and U (wt %; bottom) for all three monazite domains in the Kittelfjäll paragneiss (sample MJ18-05A). The data was obtained from geochronology analyses. **B** Results of monazite REE analysis for cores and rims, normalized to chondrite REE values (McDonough and Sun, 1995), obtained from the trace element analyses. The average Y (wt %) values for each monazite domain from the same analyses are provided. The inset plot shows the relationship between Eu anomaly (Eu*) versus Sr (ppm) for the monazite domains. **C** Results of geochronological analysis for the Kittelfjäll monazite cores presented in ^{206}Pb/^{238}U vs. ^{208}Pb/^{232}Th concordia space. The white ellipse represents the concordia age of the monazite cores. **D** Results of geochronological analysis for the Kittelfjäll monazite mantles and rims presented in ^{206}Pb/^{238}U vs. ^{208}Pb/^{232}Th concordia space. The analyses are presented together as they cannot be distinguished according to U, Th, Th/U, REE, Y, Eu*, nor Sr content. The center white ellipse represents the concordia age for all analyses, whereas the upper and lower ellipses represent the concordia ages for the ten oldest and ten youngest analyses, respectively

were partially resorbed (Waters 2001), as demonstrated by chemical maps of the garnet (Bukała et al. 2020b). Furthermore, the occurrence of kyanite intergrown with biotite in association with plagioclase (Fig. 2G), suggests that the biotite-dehydration reaction boundary was crossed during cooling to produce biotite, kyanite, and plagioclase at the

expense of garnet and K-feldspar, which has been reported for (U)HP rocks (Lang and Gilotti 2007; Kendrick and Indares 2018). The complexly zoned monazite grains are found as inclusions within both garnet and kyanite porphyroblasts and are concentrated within the matrix of biotite-kyanite domain. Their textural positions indicate that the
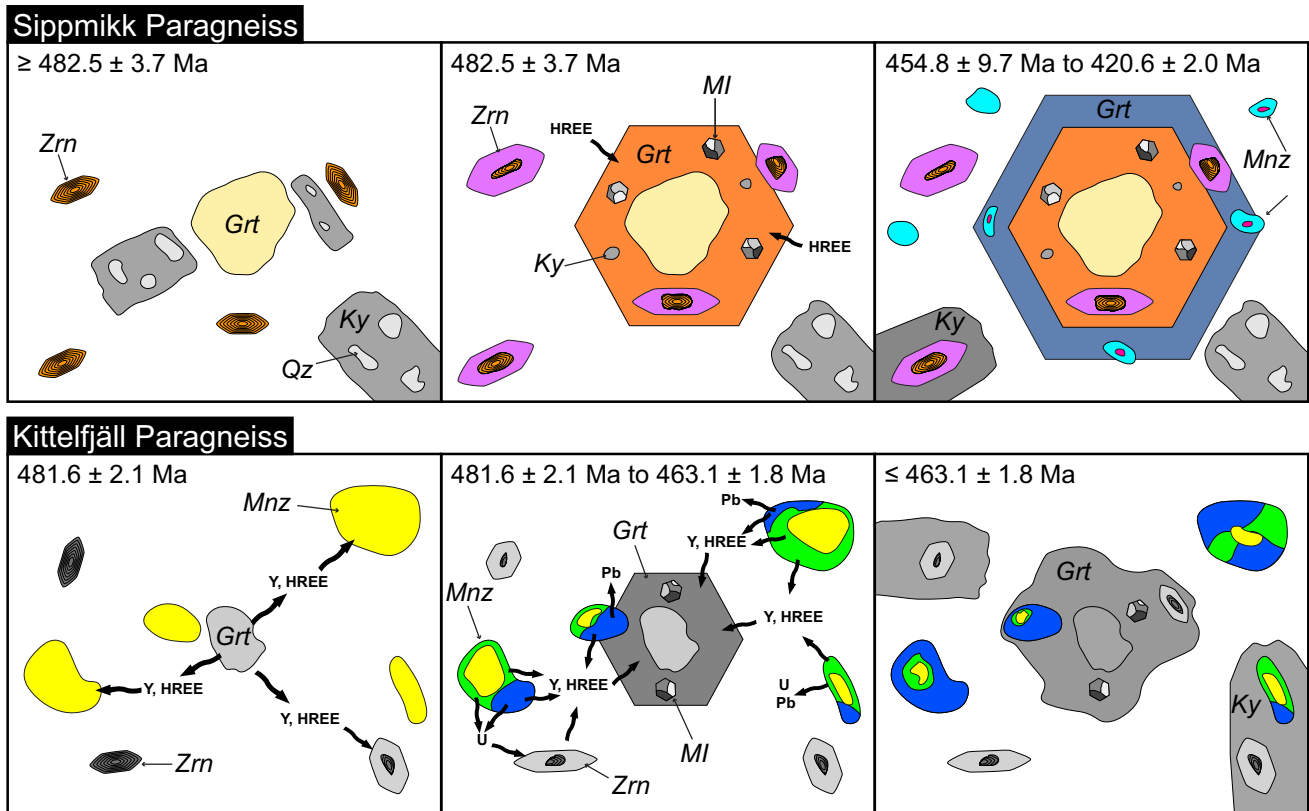
Fig. 10 Schematic summaries depicting the important metamorphic processes and the related response of zircon and monazite for the Sippmikk paragneisses (top) and the Kittelfjäll paragneiss (bottom). The coloring of the minerals is according to the color representation in previous figures, highlighting the results of this study. The coloring of garnet zones for the Sippmikk paragneiss reflects the Mn zoning pattern presented in Fig. 3 with hotter colors equaling higher Mn content. The evolution of the Sippmikk paragneiss summarized as follows: **A** Possible white mica-dehydration melting at or before 482.5 ± 3.7 Ma. Peritectic kyanite crystallizes with lobate quartz intergrowths. Garnet is partially consumed as a reactant of the melting reaction. **B** Biotite-dehydration melting at 482.5 ± 3.7 Ma. Zircon rims crystallize on the xenocrystic detrital zircon, which may have been partially resorbed during initial melting. Peritectic garnet is crystallized, trapping melt inclusions (MI), zircon, and remnants of kyanite that were formed from white mica-dehydration. HREE is sequestered by peritectic garnet. **C** Crystallization of garnet rims and a second generation of kyanite porphyroblasts, possibly occurring at 454.8 ± 9.7 Ma (i.e., the timing of (U)HP metamorphism

recorded by eclogite at Sippmikk Creek; Brueckner and Van Roermund, 2007). Monazite is captured by garnet rims and is present in the matrix. Both positions of the monazite undergo dissolution-reprecipitation at 420.6 ± 2.0 Ma. The evolution of the Kittelfjäll paragneiss is summarized as follows: **D** Possible onset of partial melting at 481.6 ± 2.1 Ma. Partial resorption of pre-existing prograde garnet porphyroblasts provides conditions to crystallize high-Y monazite, and metamorphic zircon with HREE patterns indicating absence of garnet (Bukała et al. 2020b). **E** Partial melting of the paragneiss, possibly with multiple events from 481.6 ± 2.1 Ma to 463.1 ± 1.8 Ma. Monazites undergo dissolution-reprecipitation, mediated by the melt. Biotite-dehydration melting results in the growth of peritectic garnet, which captures melt inclusions (MI) and sequesters Y and HREE from monazite and zircon. Zircon crystallization (Bukała et al. 2020b) is responsible for sequestration of U from monazite. Pb is partially lost from both mantle (yellow) and rims (blue). **F** Final crystallization of melt after 463.1 ± 1.8 Ma. Kyanite porphyroblasts are produced and entrap monazite and zircon that recorded partial melting. Garnet is partially resorbed

zoning patterns may be related to interaction with melt (Harlov et al. 2011; Weinberg et al. 2020; Ding et al. 2021).

The age of monazite core formation is established at 481.6 ± 2.1 Ma (Fig. 9C). The high Y and HREE content of the cores with respect to mantles and rims suggest that it formed in the absence of garnet, yet garnet is a major constituent of the paragneiss. Metamorphic zircon from the Kittelfjäll paragneiss show variable HREE patterns, with some suggesting dissolution of garnet during their formation, while other zircon grains indicate HREE depletion due

to garnet growth (Bukała et al. 2020b). Although the garnet chemistry does reveal distinct growth zones (Bukała et al. 2020b), it is plausible that garnet was present during the formation of the monazite cores but the relatively high Y and HREE content reflects formation during dissolution of garnet (Fig. 10; Kelly et al. 2006; Ding et al. 2021). Subsequent growth of peritectic garnet would have then provided a Y sink during mantle and rim formation (Foster et al. 2000; Pyle et al. 2001; Kohn et al. 2005; Rubatto et al. 2013). It may also be possible that monazite formed prior to any

garnet growth, however, this would not explain the HREE patterns of zircon from the paragneiss (Bukała et al. 2020b).

The chemistry of the mantles and rims are distinct from the cores but are themselves indistinguishable (Fig. 9A, B), indicating that the mantles and rims formed in similar conditions (Fig. 10). The lower U content in the mantles and rims, relative to the cores, may be a function of zircon growth in the paragneiss (Bukała et al. 2020b), whereas Y and HREE depletion indicates crystallization of the subhedral peritectic garnet (Fig. 10; Foster et al. 2000; Pyle et al. 2001; Kohn et al. 2005; Rubatto et al. 2013). Furthermore, the mantles and rims show lower Sr content and stronger Eu anomalies than the cores (Fig. 9B), which suggests crystallization of plagioclase that was not present during core formation (Holder et al. 2015), consistent with cooling during decompression and melt crystallization (Lang and Gilotti 2007; Kendrick and Indares, 2018). However, other factors may control the Eu anomalies (Holder et al. 2020).

The textures of the mantles and rims resemble formation via dissolution-reprecipitation of pre-existing monazite in the presence of melt (Harlov et al. 2011; Weinberg

et al. 2020; Ding et al. 2021). The age of 463.1 ± 1.8 Ma reflects the most complete Pb loss from the monazite and likely record the youngest episode of partial melting. Based on the association and textures of kyanite, biotite, and plagioclase (Fig. 2G), it is likely that the Kittelfjäll paragneiss cooled through the biotite-dehydration reaction boundary, consuming garnet as a result (Fig. 2F; Waters 2001; Lang and Gilotti 2007; Kendrick and Indares 2018). However, the monazite grains do not record the melt crystallization as garnet resorption should release Y and HREE to be incorporated in the monazite. Therefore, the monazite mantles and rims provide a maximum age for cooling and final melt crystallization of the paragneiss. The monazite inclusions within peritectic garnet should record an older partial melting event than those encased in kyanite. However, the oldest ages of the monazite mantles and rims are older than the monazite cores, indicating Pb re-distribution in the reprecipitated monazite volume, which obfuscates detection of older events in the inclusions. Although multiple partial melting events is suggested by re-melting of possible peritectic garnet, possibly starting at 481.6 ± 2.1 Ma, the timing of the events are

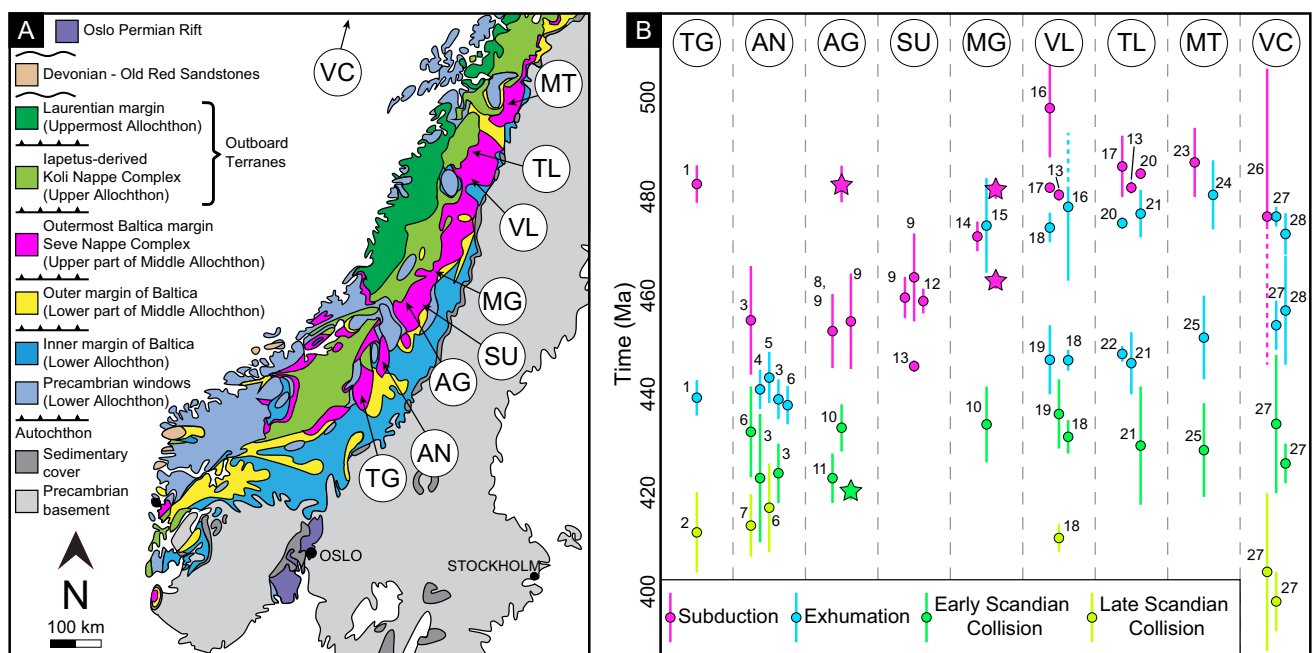

Fig. 11 A Tectonostratigraphic map of the Scandinavian Caledonides (modified after Gee et al. 2013). Key (U)HP localities of the Seve Nappe Complex are indicated across the map by the abbreviations in white circles and the Vestgötabreen Complex on Svalbard is also indicated. B Geochronological summary of the (U)HP localities in the SNC and the Vestgötabreen Complex with ages distinguished according to their original interpretation in the context of the SNC tectonic evolution. Abbreviations from left to right are: *JN* Jæren Nappe, *TG* Tväråklumparna Gneiss, *AN* Åreskutan Nappe, *AG* Avardo Gneiss, *SU* Sjouten Unit, *MG* Marsfjället Gneiss, *VL* Vaimok Lens, *TL* Tsakkok Lens, *MT* Mårma Terrane, *VC* Vestgötabreen

Complex, geochronology: [1]Walczak et al. (2021); [2]Hacker and Gans (2005); [3]Majka et al. (2012); [4]Ladenberger et al. (2014); [5]Klonowska et al. (2017); [6]Bender et al. (2019); [7]Giuntoli et al. (2020); [8]Brueckner et al. (2004); [9]Brueckner and Van Roermund (2007); [10]Grimmer et al. (2015); [11]Williams and Claesson (1987); [12]Fassmer et al. (2017); [13]Root and Corfu (2012); [14]Petrík et al. (2019); [15]Bukała et al. (2020b); [16]Barnes et al. (2019); [17]Fassmer et al. (2021); [18]Barnes et al. (2021a); [19]Dallmeyer and Gee (1986); [20]Barnes et al. (2021b); [21]Barnes et al. (2020a); [22]Dallmeyer and Stephens (1991); [23]Andréasson et al. (2018); [24]Baird et al. (2022); [25]Page (1992); [26]Bernard-Griffiths et al. (1993); [27]Barnes et al. (2020b); [28]Dallmeyer et al. (1990)

equivocal due to Pb behavior within the monazite during dissolution-reprecipitation (Seydoux-Guillaume et al. 2003; Weinberg et al. 2020; Varga et al. 2020).

Implications for the evolution of the Seve Nappe complex

The Sippmikk paragneiss (belonging to the Avardo Gneiss) and the Kittelfjäll paragneiss (belonging to the Marsfjället Gneiss) provide the first evidence for metamorphism of the central SNC in late Cambrian/early Ordovician time (Fig. 11). The P–T conditions for the partial melting events are not quantified for the Avardo and Marsfjället gneisses. However, metamorphic microdiamonds were found within the outermost regions of prograde garnet cores enveloped by peritectic garnet rims in a paragneiss near Saxnäs (belonging to the Marsfjället Gneiss), indicating UHP metamorphism prior to partial melting (Petrík et al. 2019). The timing of UHP metamorphism was interpreted to have occurred at 472 ± 3 Ma based on monazite Th–U–total Pb geochronology, yet, the monazites are characterized by a dispersion of dates defining isochron endmember ages of 479 ± 9 Ma and 460 ± 16 Ma, reflecting monazite dates of the Kittelfjäll paragneiss. Provided that partial melting in the Sippmikk paragneiss occurred at 482.5 ± 3.7 Ma, and possibly started at 481.6 ± 2.1 Ma in the Kittelfjäll paragneiss, it seems likely that the Saxnäs paragneiss underwent a similar history, inferring late Cambrian UHP metamorphism. The Sippmikk paragneiss may also have been in (U)HP conditions during or prior to partial melting, evinced by kyanite within peritectic garnet, together with two distinct generations of kyanite that are present elsewhere in the Avardo Gneiss (Van Roermund and Bakker 1983). These records reflect the evolution of the microdiamond-bearing Tväråklumparna Gneiss in the west-central SNC at 482.6 ± 3.8 Ma, either during or immediately proceeding (U)HP metamorphism (Walczak et al. 2021). Prior to the investigation of the Tväråklumparna Gneiss, late Cambrian/early Ordovician metamorphism was only identified in the northern SNC terranes as well as the Vestgöta-breen Complex on Svalbard (Fig. 11; Root and Corfu 2012; Andréasson et al. 2018; Barnes et al. 2021a, b; Fassmer et al. 2021; Baird et al. 2022). Therefore, the records of the Avardo, Marsfjället, and Tväråklumparna gneisses indicate that a larger extent of the SNC was subducted in late Cambrian/early Ordovician time and that the west-central and central SNC may have been deeper than the northern SNC.

Eclogites, peridotites, and pyroxenites have established (U)HP metamorphism of the Avardo Gneiss and the Sjouten Unit in Middle Ordovician time (Fig. 11) with general conditions of 2.3–3.0 GPa and 650–800 °C (Janák et al. 2013; Majka et al. 2014b; Gilio et al. 2015; Klonowska et al. 2016). Spinel peridotite in the Kittelfjäll paragneiss provided P–T conditions of 1–2 GPa and 650–830 °C, representing extraction from the mantle wedge during exhumation of the gneiss (Clos et al. 2014). The youngest monazite in the Kittelfjäll paragneiss indicate metamorphism proceeded until at least 463.1 ± 1.8 Ma. Considering the regional record of Middle Ordovician metamorphism, it is likely that the spinel peridotite approximates the Middle Ordovician P–T conditions of the Kittelfjäll paragneiss. The record of Middle Ordovician (U)HP metamorphism is also documented in the west-central SNC terranes (Majka et al. 2012), however, it is apparently absent from the northern SNC (Fig. 11).

No zircon and monazite investigated in this study (Figs. 7, 8, 9; Table 1) nor previous geochronological studies of the central SNC (Brueckner et al. 2004; Brueckner and Van Roermund 2007; Fassmer et al. 2017; Petrík et al. 2019) indicate Late Ordovician/early Silurian metamorphism, with the exception of zircon and rutile in eclogite belonging to the Sjouten Unit (Root and Corfu 2012; Fig. 11), which may record exhumation of the unit (Fassmer et al. 2017). The sparse Late Ordovician/early Silurian geochronological record of the central SNC contrasts both the west-central and northern SNC terranes. In the former, the rocks bear a strong record of partial melting associated with exhumation of the rocks from (U)HP conditions, recorded by zircon and monazite (Majka et al. 2012; Ladenberger et al. 2014; Klonowska et al. 2017; Walczak et al. 2021). In the latter, the rocks are characterized by deformation during exhumation in crustal conditions, recorded by white mica (Dallmeyer and Gee 1986; Dallmeyer and Stephens 1991; Page 1992; Barnes et al. 2020a, 2021b), which is also recorded in the Vestgöta-breen Complex (Fig. 11; Dallmeyer et al. 1990; Barnes et al. 2020b). All of the SNC terranes were subsequently involved in continental collision between Baltica and Laurentia in Silurian to Devonian time (Fig. 11).

In summary, the overall P–T conditions of the SNC are the highest in late Cambrian/early Ordovician time. The P–T conditions decrease progressively southwards through time with Middle Ordovician (U)HP metamorphism restricted to central/west-central SNC terranes. Subsequent Late Ordovician/early Silurian partial melting is only evident in the west-central SNC, coeval with possible subsolidus exhumation of the central SNC, and deformation in crustal levels for the northern SNC. Altogether, this pattern reflects south-to-north oblique subduction of the SNC starting in late Cambrian/early Ordovician time, followed by progressive north-to-south exhumation of the (U)HP terranes to crustal levels from early Ordovician to Late Ordovician/early Silurian time. Oblique collision from south-to-north is supported by counter-clockwise rotation of Baltica (Bottrill et al. 2014) that is reflected in its paleomagnetic record in late Cambrian time (Torsvik and Rehnström 2001; Cocks and Torsvik 2002). This evolution contrasts previous models for subduction of the SNC (e.g., Brueckner and Van Roermund 2004; Bukała et al. 2018; Fassmer et al. 2021) providing a new

basis for evaluating the closure of the Iapetus Ocean leading to continental collision of Baltica and Laurentia.

Conclusions

Zircon geochronology of the Sippmikk paragneiss (belonging to the Avardo Gneiss) resolves the timing of partial melting to 482.5 ± 3.7 Ma, likely related to biotite-dehydration. Monazite geochronology of the Sippmikk paragneiss reveals another metamorphic event at 420.6 ± 2.0 Ma, possibly overprinting a Middle Ordovician history of monazite. In the Kittelfjäll paragneiss (belonging to the Marsfjället Gneiss), relatively high-Y and low Th/U monazite cores provide a crystallization age of 481.6 ± 2.1 Ma and may be a response to resorption of garnet during initial partial melting. The monazite subsequently underwent dissolution-reprecipitation in the presence of melt, which re-equilibrated the trace element content as Y and U were sequestered by garnet and zircon, respectively. The Pb loss from monazite during dissolution-reprecipitation was less efficient, producing a spread of Th–U–Pb isotopic dates from late Cambrian to Middle Ordovician time. The youngest partial melting event that caused dissolution-reprecipitation of monazite occurred at 463.1 ± 1.8 Ma. Subsequently, the rock cooled and final melt crystallization produced biotite, kyanite, and plagioclase. The textural evidence of the paragneiss suggests that several partial melting events occurred.

The Sippmikk and Kittelfjäll paragneisses provide first evidence for late Cambrian/early Ordovician metamorphism of the central SNC. The tectonic evolutions of the paragneisses, together with geochronological and petrological studies, indicates the SNC underwent south-to-north oblique subduction in late Cambrian time, followed by progressive north-to-south exhumation to crustal levels prior to late Silurian continental collision. These results demonstrate the effectiveness for refractory minerals in metasedimentary rocks to record older histories compared to mafic and ultramafic lithologies to establish a comprehensive tectonic evolution.

Data availability All datasets can be found in the electronic supplementary material.

Declarations

References

Aleinikoff JN, Schenck WS, Plank MO et al (2006) Deciphering igneous and metamorphic events in high-grade rocks of the Wilmington complex, Delaware: morphology, cathodoluminescence and backscattered electron zoning, and SHRIMP U-Pb geochronology of zircon and monazite. Geol Soc Am Bull 118:39–64. https://doi.org/10.1130/B25659.1

Andréasson P-G (1994) The Baltoscandian margin in Neoproterozoic-early palaeozoic times. Some constraints on terrane derivation and accretion in the Arctic Scandinavian Caledonides. Tectonophysics 231:1–32

Andréasson P-G, Allen A, Aurell O et al (2018) Seve terranes of the Kebnekaise Mts., Swedish Caledonides, and their amalgamation, accretion and affinity. GFF 140:264–291. https://doi.org/10.1080/11035897.2018.1470200

Baird GB, Korhonen FJ, Chamberlain KR (2022) Pressure-temperature-deformation-time path for the Seve Nappe Complex, Kebnekaise Massif, Arctic Swedish Caledonides. In: Kuiper YD, Murphy JB, Nance RD, Strachan RA, Thompson MD (Eds) New Developments in the Appalachian-Caledonian-Variscan Orogen. Geological Society of America Special Paper 554, https://doi.org/10.1130/2021.2554(12)

Barbey P (2007) Diffusion-controlled biotite breakdown reaction textures at the solid/liquid transition in the continental crust. Contrib Mineral Petrol 154:707–716

Barnes C, Majka J, Schneider D et al (2019) High-spatial resolution dating of monazite and zircon reveals the timing of subduction–exhumation of the Vaimok Lens in the Seve Nappe Complex (Scandinavian Caledonides). Contrib Mineral Petrol. https://doi.org/10.1007/s00410-018-1539-1

Barnes CJ, Jeanneret P, Kullerud K et al (2020a) Exhumation of the high-pressure Tsäkkok Lens, Swedish Caledonides: INSIGHTS FROM THE STRUCTURAL and White Mica $^{40}Ar/^{39}Ar$ geochronological record. Tectonics 39:1–23. https://doi.org/10.1029/2020TC006242

Barnes CJ, Walczak K, Janots E et al (2020b) Timing of Paleozoic exhumation and deformation of the high-pressure Vestgötabreen complex at the Motalafjella Nunatak, Svalbard. Minerals 10:1–23. https://doi.org/10.3390/min10020125

Barnes CJ, Majka J, Jeanneret P et al (2021a) Using Th–U–Pb geochronology to extract crystallization ages of Paleozoic metamorphic monazite contaminated by initial Pb. Chem Geol 582:120450. https://doi.org/10.1016/j.chemgeo.2021.120450

Barnes C, Majka J, Schneider D, Gilio M, Alvaro M, Bukała M, Smit M (2021b) The subduction, exhumation, and deformation history of the Vaimok Lens, Seve Nappe Complex, Scandinavian Caledonides. EGU General Assembly. https://doi.org/10.5194/egusphere-egu21-8943

Bartoli O, Cesare B, Poli S et al (2013) Nanogranite inclusions in migmatitic garnet: Behavior during piston-cylinder remelting experiments. Geofluids 13:405–420. https://doi.org/10.1111/gfl.12038

Bender H, Glodny J, Ring U (2019) Absolute timing of Caledonian orogenic wedge assembly, Central Sweden, constrained by Rb–Sr multi-mineral isochron data. Lithos 344–345:339–359. https://doi.org/10.1016/j.lithos.2019.06.033

Bernard-Griffiths J, Peucat JJ, Ohta Y (1993) Age and nature of protoliths in the Caledonian blueschist-eclogite complex of western Spitsbergen: a combined approach using U-Pb, Sm–Nd and REE whole-rock systems. Lithos 30:81–90. https://doi.org/10.1016/0024-4937(93)90007-Y

Black LP, Kamo SL, Allen CM et al (2004) Improved 206Pb/238U microprobe geochronology by the monitoring of a trace-element-related matrix effect; SHRIMP, ID-TIMS, ELA-ICP-MS and oxygen isotope documentation for a series of zircon standards. Chem Geol 205:115–140. https://doi.org/10.1016/j.chemgeo.2004.01.003

Bottrill AD, van Hunen J, Cuthbert SJ, Brueckner HK, Allen MB (2014) Plate rotation during continental collision and its relations with the exhumation of UHP metamorphic terranes: Application to the Norwegian Caledonides. Geochem Geophys Geosyst 15:1766–1782. https://doi.org/10.1002/2014GC005253

Braun I, Raith M, Ravinda Kumar GR (1996) Dehydration-melting phenomena in Leptynitic Gneisses and the generation of Leucogranites: a case study from the Kerala Khondalite Belt, Southern India. J Petrol 37:1285–1305

Brueckner HK, van Roermund HLM (2004) Dunk tectonics: A multiple subduction/education model for the evolution of the Scandinavian Caledonides. Tectonics 23:1–20. https://doi.org/10.1029/2003TC001502

Brueckner HK, van Roermund HLM, Pearson NJ (2004) An Archean (?) to Paleozoic Evolution for a Garnet Peridotite Lens with Sub-Baltic Shield Affinity within the Seve Nappe Complex of Jamtland, Sweden, Central Scandinavian Caledonides. J Petrol 45:415–437. https://doi.org/10.1093/petrology/egg088

Brueckner HK, van Roermund HLM (2007) Concurrent HP metamorphism on both margins of Iapetus: Ordovician ages for eclogites and garnet pyroxenites from the Seve Nappe Complex, Swedish Caledonides. J Geol Soc London 164:117–128

Bukała M, Klonowska I, Barnes C et al (2018) UHP metamorphism recorded by phengite eclogite from the Caledonides of northern Sweden: P-T path and tectonic implications. J Metamorph Geol 36:547–566. https://doi.org/10.1111/jmg.12306

Bukała M, Barnes CJ, Jeanneret P et al (2020a) Brittle deformation during eclogitization of early Paleozoic blueschist. Front Earth Sci 8:1–17. https://doi.org/10.3389/feart.2020.594453

Bukała M, Majka J, Walczak K et al (2020b) U-Pb Zircon dating of Migmatitic paragneisses and garnet amphibolite from the high pressure Seve Nappe Complex in Kittalfjäll, Swedish Caledonides. Minerals 10:1–24. https://doi.org/10.3390/min10040295

Cesare B, Ferrero S, Salvioli-Mariani E et al (2009) "Nanogranite" and glassy inclusions: The anatectic melt in migmatites and granulites. Geology 37:627–630. https://doi.org/10.1130/G25759A.1

Cherniak DJ, Watson EB (2001) Pb diffusion in zircon. Chem Geol 172:5–24. https://doi.org/10.1016/S0009-2541(00)00233-3

Clos F, Gilio M, van Roermund HLM (2014) Fragments of deeper parts of the hanging wall mantle preserved as orogenic peridotites in the central belt of the Seve Nappe Complex, Sweden. Lithos 192–195:8–20. https://doi.org/10.1016/j.lithos.2014.01.004

Cocks LRM, Torsvik TH (2002) Earth geography from 500 to 400 million years ago: a faunal and palaeomagnetic review. J Geol Soc London 159:631–644

Corfu F, Andersen TB, Gasser D (2014) The Scandinavian Caledonides: main features, conceptual advances and critical questions. In: Corfu F, Gasser D, Chew DM (Eds) New Perspectives on the Caledonides of Scandinavia and Related Areas. Geological Society London, Special Publications 390, pp 9–43

Dallmeyer RD, Gee DG (1986) 40Ar/39Ar mineral dates from retrogressed eclogites within the Baltoscandian miogeocline: Implications for a polyphase Caledonian orogenic evolution. Geol Soc Am Bull 97:26–34

Dallmeyer RD, Gee DG (1988) Polyorogenic 40Ar/39Ar mineral age record in the Seve and Köli Nappes of the Gäddede Area, Northwestern Jämtland, Central Scandinavian Caledonides. J Geol 96:181–198

Dallmeyer RD, Peucat JJ, Hirajima T, Ohta Y (1990) Tectonothermal chronology within a blueschist-eclogite complex, west-central Spitsbergen, Svalbard: Evidence from ^{40}Ar/^{39}Ar and Rb–Sr mineral ages. Lithos 24:291–304

Dallmeyer RD, Stephens MB (1991) Chronology of eclogite retrogression within the Seve Nappe Complex, Råvvejaure, Sweden: evidence from ^{40}Ar/^{39}Ar mineral ages. Geol Runschau 80:729–743

Ding H, Kohn MJ, Zhang Z (2021) Long-lived (ca. 22–24 Myr) partial melts in the eastern Himalaya: Petrochronologic constraints and tectonic implications. Earth Planet Sci Lett 558:116764. https://doi.org/10.1016/j.epsl.2021.116764

Engi M (2017) Petrochronology Based on REE-Minerals: Monazite, Allanite, Xenotime, Apatite. In: Kohn MJ, Lanari P, Engi M (Eds) Petrochronology: Methods and Applications. Rev Mineral Petrol 83, pp 365–418

Fassmer K, Klonowska I, Walczak K et al (2017) Middle Ordovician subduction of continental crust in the Scandinavian Caledonides: an example from Tjeliken, Seve Nappe Complex, Sweden. Contrib to Mineral Petrol 172:1–21. https://doi.org/10.1007/s00410-017-1420-7

Fassmer K, Froitzheim N, Janák M et al (2021) Diachronous collision in the Seve Nappe Complex: evidence from Lu-Hf geochronology of eclogites (Norrbotten, North Sweden). J Metamorph Geol 39:819–842. https://doi.org/10.1111/jmg.12591

Ferrero S, Bartoli O, Cesare B et al (2012) Microstructures of melt inclusions in anatectic metasedimentary rocks. J Metamorph Geol 30:303–322. https://doi.org/10.1111/j.1525-1314.2011.00968.x

Ferrero S, Wunder B, Walczak K et al (2015) Preserved near ultrahigh-pressure melt from continental crust subducted to mantle depths. Geology 43:447–450. https://doi.org/10.1130/G36534.1

Fitzsimons ICW (1996) Metapelitic Migmatites from Brattstrant Bluffs, East Antarctica – Metamorphism, Melting and Exhumation of Mid Crust. J Petrol 37:395–414

Foster G, Kinny P, Vance D et al (2000) The significance of monazite U-Th-Pb age data in metamorphic assemblages; a combined study of monazite and garnet chronometry. Earth Planet Sci Lett 181:327–340

Gee DG, Guezou J-C, Roberts D, Wolff FC (1985) The central-southern part of the Scandinavian Caledonides. In: Gee DG, Sturt BA (eds) The Caledonide Orogen -Scandinavia and Related Areas. John Wiley & Sons Inc, pp 109–133

Gee DG, Fossen H, Henriksen N, Higgins AK (2008) From the early Paleozoic platforms of Baltica and Laurentia to the Caledonide Orogen of Scandinavia and Greenland. Episodes 31:44–51. https://doi.org/10.18814/epiiugs/2008/v31i1/007

Gee DG, Janák M, Majka J et al (2013) Subduction along and within the Baltoscandian margin during closing of the Iapetus Ocean and Baltica-Laurentia collision. Lithosphere 5:169–178. https://doi.org/10.1130/L220.1

Gee DG, Klonowska I, Andréasson P-G, Stephens MB (2020) Middle thrust sheets in the Caledonide orogen, Sweden: The outer margin of Baltica, the continent-ocean transition zone and late Cambrian-Ordovician subduction-accretion. In: Stephens MB, Wiehed JB (eds) Sweden: Lithotectonic Framework. Tectonic Evolution and Mineral Resources, Geological Society, London, Memoirs, pp 517–548

Gilio M, Clos F, van Roermund HLM (2015) The Friningen Garnet Peridotite (central Swedish Caledonides). A good example of the characteristic PTt path of a cold mantle wedge garnet peridotite. Lithos 230:1–16. https://doi.org/10.1016/j.lithos.2015.05.003

Giuntoli F, Menegon L, Warren CJ et al (2020) Protracted Shearing at Midcrustal Conditions During Large-Scale Thrusting in the Scandinavian Caledonides. Tectonics 39:1–31. https://doi.org/10.1029/2020TC006267

Grimmer JC, Glodny J, Drüppel K et al (2015) Early- to mid-Silurian extrusion wedge tectonics in the central Scandinavian Caledonides. Geology 43:347–350. https://doi.org/10.1130/G36433.1

Hacker BR, Gans PB (2005) Continental collisions and the creation of ultrahigh-pressure terranes: Petrology and thermochronology of nappes in the central Scandinavian Caledonides. GSA Bull 117:117–134. https://doi.org/10.1130/B25549.1

Harley SL, Kelly NM, Möller A (2007) Zircon behaviour and the thermal histories of mountain chains. Elements 3:25–30. https://doi.org/10.2113/gselements.3.1.25

Harlov DE, Wirth R, Hetherington CJ (2011) Fluid-mediated partial alteration in monazite: the role of coupled dissolution–reprecipitation in element redistribution and mass transfer. Contrib to Mineral Petrol 162:329–348. https://doi.org/10.1007/s00410-010-0599-7

Hermann J, Rubatto D (2003) Relating zircon and monazite domains to garnet growth zones: Age and duration of granulite facies metamorphism in the Val Malenco lower crust. J Metamorph Geol 21:833–852. https://doi.org/10.1046/j.1525-1314.2003.00484.x

Hokada T, Harley SL (2004) Zircon growth in UHT leucosome: constraints from zircon garnet rare earth elements (REE) relations in Napier Complex, East Antarctica. J Mineral Petrol Sci 99:180–190

Holder RM, Hacker BR, Kylander-Clark ARC, Cottle JM (2015) Monazite trace-element and isotopic signatures of (ultra) high-pressure metamorphism: Examples from the Western Gneiss Region, Norway. Chem Geol 409:99–111

Holder RM, Yakymchuk C, Viete DR (2020) Accessory Mineral Eu Anomalies in Suprasolidus Rocks: Beyond Feldspar. Geochem Geophys Geosyst 21:e2020GC009052. https://doi.org/10.1029/2020GC009052

Indares A, Dunning G (2001) Partial melting of high-P–T Metapelites from the Tshenukutish Terrane (Grenville Province): Petrography and U-Pb Geochronology. J Petrol 42:1547–1565

Jackson SE, Pearson NJ, Griffin WL, Belousova EA (2004) The application of laser ablation-inductively coupled plasma-mass spectrometry to in situ U-Pb zircon geochronology. Chem Geol 211:47–69. https://doi.org/10.1016/j.chemgeo.2004.06.017

Janák M, Van Roermund H, Majka J, Gee D (2013) UHP metamorphism recorded by kyanite-bearing eclogite in the Seve Nappe Complex of northern Jämtland, Swedish Caledonides. Gondwana Res 23:865–879. https://doi.org/10.1016/j.gr.2012.06.012

Kelly NM, Clarke GL, Harley SL (2006) Monazite behaviour and age significance in poly-metamorphic high-grade terrains: A case study from the western Musgrave Block, central Australia. Lithos 88:100–134. https://doi.org/10.1016/j.lithos.2005.08.007

Kendrick J, Indares A (2018) The reaction history of kyanite in high-P aluminous granulites. J Metamorph Geol 36:125–146. https://doi.org/10.1111/jmg.12286

Klonowska I, Janák M, Majka J et al (2016) Eclogite and garnet pyroxenite from Stor Jougdan, Seve Nappe Complex, Sweden: Implications for UHP metamorphism of allochthons in the Scandinavian Caledonides. J Metamorph Geol 34:103–119. https://doi.org/10.1111/jmg.12173

Klonowska I, Janák M, Majka J et al (2017) Microdiamond on Åreskutan confirms regional UHP metamorphism in the Seve Nappe Complex of the Scandinavian Caledonides. J Metamorph Geol 35:541–564. https://doi.org/10.1111/jmg.12244

Kohn MJ, Wieland MS, Parkinson CD, Upreti BN (2005) Five generations of monazite in Langtang gneisses: implications for chronology of the Himalayan metamorphic core. J Metamorph Geol 23:399–406. https://doi.org/10.1111/j.1525-1314.2005.00584.x

Ladenberger A, Be'eri-Shlevin Y, Claesson S, et al (2014) Åreskutan Nappe – Caledonian Tectonometamorphic evolution of the A history revealed by SIMS U–Pb zircon geochronology. In: Corfu F, Gasser D, Chew DM (eds) New Perspectives on the Caledonides of Scandinavia and Related Areas. Geological Society London 390, Special Publications, pp 337–368

Lang HM, Gilotti JA (2007) Partial melting of metapelites at ultrahigh-pressure conditions, Greenland Caledonides. J Metamorph Geol 25:129–147. https://doi.org/10.1111/j.1525-1314.2006.00687.x

Lanzirotti A (1995) Yttrium zoning in metamorphic garnets. Geochemica Cosmochim Acta 59:4105–4110

Liu P, Wu Y, Liu Q et al (2014) Partial melting of UHP calc-gneiss from the Dabie Mountains. Lithos 192–195:86–101. https://doi.org/10.1016/j.lithos.2014.01.012

Majka J, Be'eri-Shlevin Y, Gee DG et al (2012) Multiple monazite growth in the Åreskutan migmatite: Evidence for a polymetamorphic Late Ordovician to Late Silurian evolution in the Seve Nappe Complex of west-central Jämtland, Sweden. J Geosci 57:3–23. https://doi.org/10.3190/jgeosci.112

Majka J, Rosén Å, Janák M et al (2014a) Microdiamond discovered in the Seve Nappe (Scandinavian Caledonides) and its exhumation by the "vacuum-cleaner" mechanism. Geology 42:1107–1110. https://doi.org/10.1130/G36108.1

Majka J, Janák M, Andersson B, et al (2014b) Pressure-temperature estimates on the Tjeliken eclogite: New insights into the (ultra)-high-pressure evolution of the Seve Nappe Complex in the Scandinavian Caledonides. In: Corfu F, Gasser D, Chew DM (Eds) New Perspectives on the Caledonides of Scandinavia and Related Areas, Geological Society London, Special Publications 390, pp 369–384

McDonough WF, Sun S-s (1995) The composition of the Earth. Chem Geol 120:223–253. https://doi.org/10.1016/0009-2541(94)00140-4

Page LM (1992) $^{40}Ar/^{39}Ar$ geochronological constraints on timing of deformation and metamorphism of the Central Norrbotten Caledonides, Sweden. Geol J 27:127–150. https://doi.org/10.1002/gj.3350270204

Paquette JL, Tiepolo M (2007) High resolution (5 μm) U-Th-Pb isotope dating of monazite with excimer laser ablation (ELA)-ICPMS. Chem Geol 240:222–237. https://doi.org/10.1016/j.chemgeo.2007.02.014

Perchuk AL, Burchard M, Maresch WV, Schertl HP (2008) Melting of hydrous and carbonate mineral inclusions in garnet host during ultrahigh pressure experiments. Lithos 103:25–45. https://doi.org/10.1016/j.lithos.2007.09.008

Perchuk AL, Burchard M, Maresch WV, Schertl H-P (2005) Fluid-mediated modification of garnet interiors under ultrahigh-pressure conditions. Terra Nov 17:545–553. https://doi.org/10.1111/j.1365-3121.2005.00647.x

Petrík I, Janák M, Klonowska I et al (2019) Monazite behaviour during metamorphic evolution of a diamond-bearing gneiss: a case study from the Seve Nappe Complex, Scandinavian Caledonides. J Petrol 60:1773–1796. https://doi.org/10.1093/petrology/egz051

Petrus JA, Kamber BS (2012) VizualAge: A Novel Approach to Laser Ablation ICP-MS U-Pb Geochronology Data Reduction. Geostand Geoanalytical Res 36:247–270. https://doi.org/10.1111/j.1751-908X.2012.00158.x

Pyle JM, Spear FS, Rudnick RL, McDonough WF (2001) Monazite-Xenotime-Garnet Equilibrium in Metapelites and a New Monazite-Garnet Thermometer. J Petrol 42:2083–2107

Pyle JM, Spear FS (2003) Yttrium zoning in garnet: Coupling of major and accessory phases during metamorphic reactions. Am Mineral 88:708

Roberts D (2003) The Scandinavian Caledonides: event chronology, palaeogeographic settings and likely modern analogues. Tectonophysics 365:283–299. https://doi.org/10.1016/S0040-1951(03)00026-X

Root D, Corfu F (2012) U-Pb geochronology of two discrete Ordovician high-pressure metamorphic events in the Seve Nappe Complex, Scandinavian Caledonides. Contrib to Mineral Petrol 163:769–788. https://doi.org/10.1007/s00410-011-0698-0

Rubatto D (2002) Zircon trace element geochemistry: partitioning with garnet and the link between U-Pb ages and metamorphism. Chem Geol 184:123–138

Rubatto D, Chakraborty S, Dasgupta S (2013) Timescales of crustal melting in the Higher Himalayan crystallines (Sikkim, Eastern Himalaya) inferred from trace element-constrained monazite and zircon chronology. Contrib to Mineral Petrol 165:349–372. https://doi.org/10.1007/s00410-012-0812-y

Rubatto D (2017) Zircon: The Metamorphic Mineral. In: Kohn MJ, Lanari P, Engi M (Eds) Petrochronology: Methods and Applications. Rev Mineral Petrol 83, pp 261–295

Seydoux-Guillaume AM, Goncalves P, Wirth R, Deutsch A (2003) Transmission electron microscope study of polyphase and discordant monazites: Site-specific specimen preparation using the focused ion beam technique. Geology 31:973–976. https://doi.org/10.1130/G19582.1

Sláma J, Košler J, Condon DJ et al (2008) Plešovice zircon — A new natural reference material for U-Pb and Hf isotopic microanalysis. Chem Geol 249:1–35. https://doi.org/10.1016/j.chemgeo.2007.11.005

Stephens MB, Gee DG (1985) A tectonic model for the evolution of the eugeoclinal terranes in the central Scandinavian Caledonides. In: Gee DG, Sturt BA (eds) The Caledonide Orogen -Scandinavia and Related Areas. John Wiley & Sons Inc, pp 953–978

Stephens MB (1988) The Scandinavian Caledonides: a complexity of collisions. Geol Today 4:20–26

Stephens MB (2020) Upper and uppermost thrust sheets in the Caledonide orogen, Sweden: outboard oceanic and exotic continental terranes. In: Stephens MB, Wiehed JB (eds) Sweden: Lithotectonic Framework. Tectonic Evolution and Mineral Resources, Geological Society, London, Memoirs, pp 549–575

Symmes GH, Ferry JM (1992) The effect of whole-rock MnO content on the stability of garnet in pelitic schists during metamorphism. J Metamorpic Geol 10:221–237

Szopa K, Kusiak M, Gawęda A et al (2017) Monazite-(Ce) from the Skalna Brama Pegmatite, Sudety Mts, Poland, as potentially new reference material for U-Pb geochronology. NGF Abstr Proc 2:143–144

Torsvik TH, Rehnström EF (2001) Palaeomagnetic data from Baltica: implications for true polar wander and Cambrian palaeogeography. J Geol Soc London 158:321–329

Trouw RAJ (1973) Structural Geology of the Marsfjällen Area Caledonidea of Västerbotten, Sweden. Sveriges Geol Unders 67:1–121

Van Roermund HLM, Bakker E (1983) Structure and metamorphism of the Tången—Inviken area, Seve Nappes, Central Scandinavian Caledonides. Geol Föreningen i Stock Förhandlingar 105:301–319. https://doi.org/10.1080/11035898309454568

Van Roermund HLM (1985) Eclogites of the Seve Nappe, central Scandinavian Caledonides. In: Gee DG, Sturt BA (eds) The Caledonide Orogen -Scandinavia and Related Areas. John Wiley & Sons Inc, pp 873–888

Van Roermund HLM (1989) High-pressure ultramafic rocks from the Allochthonous Nappes of the Swedish Caledonides. In: Caledonide T (ed) Gayer RA. Springer, Geology of Scandinavia, pp 205–219

Varga J, Raimondo T, Daczko NR, Adam J (2020) Experimental alteration of monazite in granitic melt: Variable U-Th–Pb and REE mobility during melt-mediated coupled dissolution-precipitation. Chem Geol 544:119602. https://doi.org/10.1016/j.chemgeo.2020.119602

Vermeesch P (2018) Geoscience Frontiers IsoplotR: a free and open toolbox for geochronology. Geosci Front 9:1479–1493. https://doi.org/10.1016/j.gsf.2018.04.001

Vermeesch P (2020) Unifying the U-Pb and Th–Pb methods: joint isochron regression and common Pb correction. Geochronology 2:119–131. https://doi.org/10.5194/gchron-2-119-2020

Walczak K, Barnes CJ, Majka J et al (2021) Zircon age depth-profiling sheds light on the early Caledonian evolution of the Seve Nappe Complex in west-central Jämtland. Geosci Front. https://doi.org/10.1016/j.gsf.2020.11.009

Waters DJ (2001) The significance of prograde and retrograde quartz-bearing intergrowth microstructures in partially melted granulite-facies rocks. Lithos 56:97–110

Weinberg RF, Wolfram LC, Nebel O et al (2020) Decoupled U-Pb date and chemical zonation of monazite in migmatites: The case for disturbance of isotopic systematics by coupled dissolution-reprecipitation. Geochim Cosmochim Acta 269:398–412. https://doi.org/10.1016/j.gca.2019.10.024

Whitehouse MJ, Platt JP (2003) Dating high-grade metamorphism - Constraints from rare-earth elements in zircon and garnet. Contrib to Mineral Petrol 145:61–74. https://doi.org/10.1007/s00410-002-0432-z

Whitney DL, Evans BW (2010) Abbreviations for names of rock-forming minerals. Am Mineral 95:185–187. https://doi.org/10.2138/am.2010.3371

Wiedenbeck M, Hanchar JM, Peck WH et al (2004) Further characterisation of the 91500 Zircon Crystal. Geostand Geoanalytical Res 28:9–39

Williams PF, Zwart HJ (1977) A Model for the Development of the Seve-Köli Caledonian Nappe Complex. In: Saxena SK, Bhattacharji S, Annersten H, Stephansson O (eds) Energetics of Geological Processes. Springer, pp 169–187

Williams IS, Claesson S (1987) Isotopic evidence for the Precambrian provenance and Caledonian metamorphism of high grade paragneisses from the Seve Nappes, Scandinavian Caledonides II. Ion microprobe zircon U-Th-Pb. Contrib to Mineral Petrol 97:205–217

Xia Q-X, Wang H, Zhou L-G et al (2016) Growth of metamorphic and peritectic garnets in ultrahigh-pressure metagranite during continental subduction and exhumation in the Dabie orogen. Lithos 266–267:158–181. https://doi.org/10.1016/j.lithos.2016.08.043

Xia Q-X, Zhou L-G (2017) Different origins of garnet in high pressure to ultrahigh pressure metamorphic rocks. J Asian Earth Sci 145:130–148. https://doi.org/10.1016/j.jseaes.2017.03.037

Zachrisson E, Sjöstrand T (1990) Berggrundskartorna 22E Frostviken 1:50000. Sveriges Geol Undersökning Ai 41–44